

Stephan Glögger

Development of an Algorithm to Determine the Total Radiated Power

IPP 2018-06
März 2018



ulm university universität
uulm



Max-Planck-Institut
für Plasmaphysik

Masterarbeit

**Development of an Algorithm
to Determine the
Total Radiated Power**

Stephan Glögler

Oktober 2015

Development of an Algorithm to Determine the Total Radiated Power
Entwicklung eines Algorithmus zur Bestimmung der gesamt abgestrahlten Leistung

Vorgelegt von: Stephan Glöggler, geb. 05.06.1991 in Ulm-Söflingen

Matrikelnummer: 697447

E-Mail: stephan.gloeggler@uni-ulm.de
stephan.gloeggler@ipp.mpg.de

1. Prüfer: Prof. Dr. Frank Jenko

2. Prüfer: Dr. Thomas Eich

Betreuer: Dr. Matthias Bernert

Selbstständigkeitserklärung

Hiermit erkläre ich, diese Masterarbeit selbstständig erarbeitet und verfasst und hierzu keine anderen als die angegebenen Quellen verwendet zu haben.

(Stephan Glöggler)

Abstract

Radiation is an essential part of the power balance in a fusion plasma. In future fusion devices, such as ITER or DEMO, up to 95% of the power will have to be dissipated, mainly by radiation. For the development of an appropriate operational scenario, information about the plasma radiation's level ($P_{rad,tot}$) and distribution is crucial. In order to obtain this information, bolometers are used. As the bolometers can only provide a line-integrated measurement of the plasma radiation, it is necessary to invert those measurements. At ASDEX Upgrade, the Anisotropic Diffusion Model Tomography is used to reconstruct the poloidal radiation distribution. For the calculation of a time trace of $P_{rad,tot}$ the faster BPD algorithm is used.

After many years in operation, this algorithm is not suited anymore for the present plasma properties. In this thesis a new algorithm for the calculation of $P_{rad,tot}$ is implemented. It applies an Abel inversion on the main chamber and introduces empirically based assumptions for poloidal asymmetries and the divertor radiation. To benchmark the new algorithm, synthetic emissivity profiles are used. The program introduced in this thesis is used to create a set of synthetic poloidal emissivity profiles and to calculate out of this the synthetic measurements of the bolometry. On average, the new Abel inversion based algorithm deviates by only 10% from the nominal synthetic value while the BPD is about 25% too low. Further examination reveals that the BPD algorithm underestimates the divertor radiation. Furthermore, time traces of complete ASDEX Upgrade shots are calculated. The analysis of these time traces shows that the underestimation of the divertor radiation can have significant consequences on the accuracy of the BPD while the new Abel inversion based algorithm is shown to be stable.

Contents

1	Introduction	1
1.1	Nuclear Fusion	1
1.2	Magnetic Confinement	2
1.3	The Tokamak ASDEX Upgrade	3
1.4	Motivation	5
2	Plasma Radiation and Bolometry	7
2.1	Plasma Radiation	7
2.1.1	Radiation Processes	7
2.1.2	Intrinsic Radiation in a Tokamak	9
2.1.3	Cooling Factor	10
2.1.4	Impurity Seeding	11
2.2	Foil Bolometers	13
3	Determining the Total Radiated Power	19
3.1	Reconstruction of the Magnetic Flux Surfaces	19
3.2	Tomography	20
3.2.1	The Radon Transform	20
3.2.2	Transform Methods	21
3.2.3	Series Expansion Methods	23
3.2.4	Constrained Optimization	24
3.2.5	Anisotropic Diffusion Model Tomography	26
3.3	The BPD Algorithm	29
3.4	Abel Inversion Based Algorithm	31
3.4.1	Abel Inversion	31

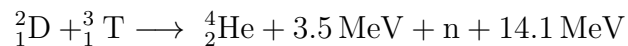
Contents

3.4.2	Slice-and-Stack Method	32
3.4.3	Implementation at ASDEX Upgrade	33
3.4.4	Corrections in the SOL	36
3.4.5	Approach for the Divertor	38
3.4.6	Further Development	41
4	Benchmarking and Application	43
4.1	Synthetic Emissivity Profile Program	43
4.1.1	Creation of the Profiles	43
4.1.2	Calculation of the Lines of Sight Measurements	45
4.2	Evaluation of Several Synthetic Emissivity Profiles	47
4.2.1	Evaluation of Single Profiles	48
4.2.2	Statistical Evaluation	51
4.3	Error Mapping	55
4.4	Application: Time Traces	56
4.4.1	Time Trace of Shot 31113	57
4.4.2	Time Trace of Shot 31295	58
4.4.3	Time Trace of Shot 30503	59
5	Summary and Conclusion	63
5.1	Outlook	66
A	Bibliography	67
B	Synthetic Emissivity Profiles	71
C	Synthetic Bolometry Manual	83
	Acknowledgements	107

1 Introduction

1.1 Nuclear Fusion

The world's power supply is facing various challenges. To ensure a stable and sustainable energy production, new sources of energy are necessary. One promising candidate is nuclear fusion. Considering the required conditions, the fusion processes taking place in the core of the sun are difficult to realize in a laboratory or a reactor. The most practicable fusion reaction on earth is the fusion of deuterium and tritium [1]:



The temperature with the most fusion reactions is at around 10 keV (~ 100 million K). At such high temperatures the involved components are ionized, i.e. in the state of a plasma.

An advantage of this reaction is the availability of the reactants. Deuterium can be extracted from water whereas tritium has to be bred from lithium. Both substances occur plentiful on our planet. The helium created from this reaction is not only harmless, it can further heat up the plasma with its part of the reaction energy, whilst the neutrons can be used to breed new tritium. As yet, the necessary technical and physical conditions for an economically feasible fusion power plant have not been achieved.

1.2 Magnetic Confinement

It would be impossible for any surrounding material to withstand direct contact with the hot plasma. Therefore, a magnetic field is used to confine the plasma. The Lorentz force leads to a gyration movement of the charged plasma particles around the magnetic field lines. One configuration using this principle is the torus-shaped tokamak (see fig. 1.1). The field lines in toroidal direction are generated by external magnetic field coils. Since drift movements would make this configuration unable to confine the plasma, a second poloidal field is needed to stabilize it. The poloidal field is generated by the plasma current, flowing in toroidal direction. The electric field that is driving this current is induced by a solenoid in the hole of the torus, serving as the primary winding of a transformer, of which the plasma acts as the secondary winding. In the poloidal cross-section, the magnetic field on the inner side (lower major radius) is higher as on the outer side. Therefore they are referred to as high field side (HFS) and low field side (LFS).

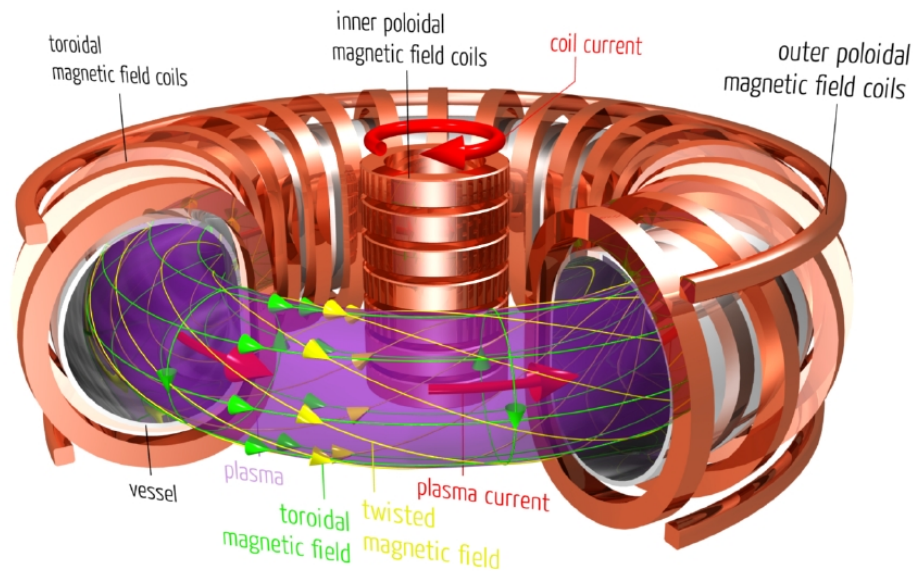


Fig. 1.1: Basic principle of a tokamak. Taken from [2].

As the current in the solenoid can not be infinitely increased due to technical limits, for now a tokamak can not be operated steady-state but only in pulsed operation (one discharge process is called a shot). In the other main concept for a thermonuclear fusion reactor, the stellarator, the poloidal magnetic field is produced by complexly ordered external coils, therefore it doesn't need a plasma current that has to be driven and could run steady-state. It will have to be examined during the next decades which concept turns out to be more favorable.

1.3 The Tokamak ASDEX Upgrade

ASDEX Upgrade (AUG) is a tokamak, operated by the Max Planck Institute for Plasma Physics in Garching, Germany, since 1991. Its main purpose is to examine the physics underlying the operation of future fusion reactors, such as ITER which is currently under construction in Cadarache, France. Having a major radius of 1.60 m and a minor radius of 0.50 m, ASDEX Upgrade is a so called medium-sized tokamak. Its size and other plasma parameters (see Table 1.1) are not sufficient to produce a burning plasma (i.e. it can not sustain itself without additional heating). Though, some parameters as density, pressure, and the wall design are similar to the ones expected in a fusion power plant.

Table 1.1: Main parameters of ASDEX Upgrade [3]

Major radius	1.60 m
Minor radius	0.50 m
Plasma volume	13 m ³
Magnetic field	up to 3.9 T
Plasma current	2 MA
Plasma heating	27 MW
Pulse length	10 s
Plasma density	$20 \cdot 10^{20} \text{ m}^{-3}$
Plasma temperature	10 keV

1 Introduction

The experiments are performed using hydrogen, deuterium, and helium plasmas. The above mentioned deuterium-tritium mix is not used in order to avoid safety issues related to the tritium's radioactivity.

The name ASDEX Upgrade is an acronym for **Axial Symmetric Divertor EX**periment which indicates that the tokamak is operated with a divertor configuration. In the limiter configuration, where the last closed flux surface is defined by the first wall, not only the energy from the plasma center is deposited directly onto the wall but also impurity particles that are sputtered out of the wall can easily enter the confined plasma. In the divertor configuration an additional poloidal magnetic field is added so that the last closed flux surface now strikes the wall only on special divertor plates (see fig. 1.2), far from the core plasma where the nuclear reactions take place.

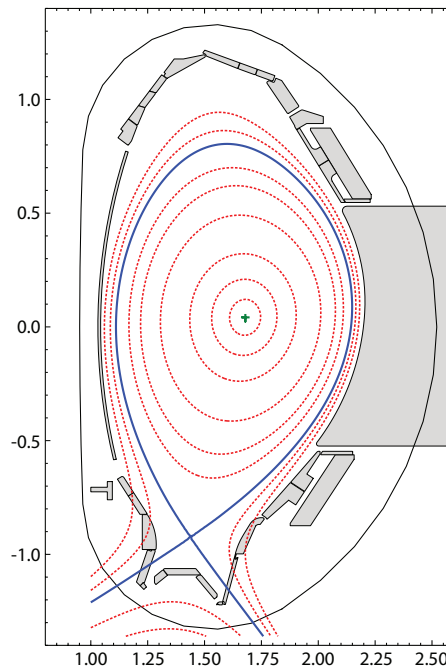


Fig. 1.2: Poloidal cross-section of ASDEX Upgrade with flux surface lines (red), separatrix (blue) and magnetic axis (green). The flux surfaces inside the separatrix are closed while the flux surfaces outside the separatrix intersect with the first wall.

As a result of the altered magnetic field, a null-point, the so-called X-point, has formed. It can be located either on top (upper single null) or at the bottom (lower single null) of the plasma or even both (double null). The flux surface through the X-point, called separatrix, separates the poloidal cross-section of the tokamak into the confined plasma where the flux surfaces are closed and the region of flux surfaces that will intercept the wall or the divertor plates. The particles in that region, called the scrape-off-layer (SOL) for this reason, will hence be leaving the plasma. The plasma particles hitting the divertor plates at the so-called strike points are neutralized and can be pumped out of the reactor more easily.

As the charged particles primarily move along the magnetic field lines, the physical properties along the magnetic field lines (and therefore on the flux surfaces) are more similar than perpendicular to them. One can define a relative coordinate on the poloidal magnetic field to take this behavior into account. This coordinate is defined as

$$\rho_{pol}(\Psi) = \sqrt{\frac{\Psi - \Psi_c}{\Psi_s - \Psi_c}} \quad (1.1)$$

where Ψ_c is the poloidal magnetic flux of the magnetic axis (the center or core) and Ψ_s the magnetic flux of the separatrix. I.e. on the magnetic axis $\rho_{pol,c} = 0$ and on the separatrix $\rho_{pol,s} = 1$. The region with a $\rho_{pol} > 0.9$ is called the plasma edge.

1.4 Motivation

Even the most resistive divertor plate material will not withstand the continuous power deposition by incoming particles in a future reactor and it is necessary to dissipate a major fraction of that power in the plasma edge by radiation before it can harm the divertor plates. As the intrinsic plasma radiation will not be sufficient for this purpose, it is necessary to introduce impurity particles into the plasma. While in the SOL additional radiation from impurities is desirable, impurities are

1 Introduction

unwanted in the plasma core since they are good radiators and lead to a power loss by radiation. The quantity and location of plasma radiation is therefore an essential piece of information for the operation of a tokamak, not only to protect the divertor plates but also because radiation is one of the main power dissipation channels. For future reactors it will be necessary to increase the fraction of radiated power. Furthermore, information about plasma radiation serves to understand and control the behavior of impurities, transport processes, disruptions, and detachment [4]. The main parameter for the power balance is the total radiated power $P_{rad,tot}$. At ASDEX Upgrade $P_{rad,tot}$ is calculated by an algorithm using measurements of the foil bolometer system. As the current algorithm turned out to be not adequate anymore, this thesis aims to develop a new algorithm for $P_{rad,tot}$, based on an adjusted Abel Inversion. Furthermore, the new algorithm was tested and benchmarked with synthetic emissivity profiles.

Chapter 2 will present the most common types of radiation and in which regions of the plasma they will have to be considered. It will also give an introduction to the functioning of foil bolometers which are capable of measuring a wide range of the radiation spectrum. It is not trivial to determine the emissivity distribution from these measurements since mathematically it is an ill-posed problem. Chapter 3 will give a short overview over the possibilities to tackle this problem and will especially introduce the basics of the algorithms that are used at ASDEX Upgrade to determine the emissivity distribution and $P_{rad,tot}$. It will also introduce the new $P_{rad,tot}$ algorithm, which was developed during this thesis' work, and its underlying assumptions. The evaluation of the different codes using synthetic emissivity profiles, that are introduced in this thesis, will be discussed in chapter 4. A summary and outlook is given in chapter 5.

2 Plasma Radiation and Bolometry

Radiation is one of the main power dissipation channels of a fusion plasma. In a plasma, different sources of radiation can be found, depending on the local conditions and each with its respective radiation characteristics. Each fusion device has an intrinsic radiation, but it can be advantageous to increase the radiation power and alter its location in the tokamak by seeding impurity gases into the plasma. For the stability of the plasma and the safety of the reactor components it is important to determine the radiative power emitted by a plasma. This can be done with bolometers which are able to detect the incident power of a wide range of the electromagnetic spectrum [5].

2.1 Plasma Radiation

The types of radiation that occur in a tokamak plasma depend strongly on the local electron temperature and the density. An important role is also played by impurities in the plasma which are eroded from the wall material and are deliberately seeded into the plasma.

2.1.1 Radiation Processes

There are different processes in a plasma that produce radiation. The dominating processes are the following:

Line radiation: An electron bound in a neutral or partially ionized atom can be excited into a higher energetic state E_j by collisions. The following spontaneous de-excitation of the excited electron into a lower energetic state E_i leads to the emission of a photon with energy $\Delta E = E_j - E_i$, corresponding to the wavelength $\nu = \Delta E/h$ (h being the Planck constant). As the energy states vary for every atomic species, the wavelength of an emitted photon is characteristic. A spectral line can be observed and also used for diagnostic purposes.

Bremsstrahlung: Electrons that are accelerated in the electric field of partially or fully ionized impurity ions emit bremsstrahlung. The radiation spectrum of bremsstrahlung is continuous. The power dissipated by Bremsstrahlung of electrons that are scattered at ions of charge Z can be expressed as [1]

$$P_{br} = c Z^2 n_e n_Z T_e^{1/2} \quad (2.1)$$

with $c = 5.35 \cdot 10^{-37} \text{ Wm}^{-3}$, n_e the electron density, n_Z the density of impurities of charge Z and the electron temperature T_e . In order to describe a plasma with multiple kinds of impurity ions, one can substitute the Z in eq. (2.1) with an effective charge

$$Z_{eff} = \sum_Z n_Z Z^2 / n_e \quad (2.2)$$

with $n_e = \sum_Z Z n_Z$. As bremsstrahlung requires ionized particles it will occur mostly in the confined region of the plasma because here n_e , n_Z and T_e are high.

Recombination radiation: A free electron can be captured by an ion and occupy one of the possible energy states within the ion. The excess power of the electron is dissipated by radiation. The radiation spectrum is therefore continuous but has ion-specific resonance peaks. This kind of radiation will

mostly occur in the plasma edge due to the low temperatures, for high Z impurities also further central.

Other types of radiation, e.g. cyclotron radiation, occur as well. They can be used for diagnostic and heating purposes but their contribution to the total power loss by radiation is negligible.

2.1.2 Intrinsic Radiation in a Tokamak

A tokamak plasma can be roughly divided in two main regions: the confined plasma, where the highest temperatures are achieved, and the edge, where in standard cases most of the plasma's power is dissipated.

In the core the electron temperature and the density are very high ($T_e \approx 10$ keV, $n_e \approx 1 \cdot 10^{19} - 2 \cdot 10^{20} \text{m}^{-3}$). Therefore, according to eq. (2.1), Bremsstrahlung (in the soft X-ray range) is dominating in standard scenarios. As in the plasma core a high T_e is required in order to induce further fusion reactions, the power dissipated by radiation in this region is required to be low. As the radiated power of Bremsstrahlung increases quadratically with Z_{eff} , the amount of impurities with a high Z has to be kept as low as possible. The maximum tolerable abundances are $< 3 \cdot 10^{-2}$ for carbon and $< 2 \cdot 10^{-4}$ for tungsten (an influence on the operation can already be observed for lower concentrations, though) [6]. For heavy impurities (e.g. tungsten from the first wall) there is also line radiation and recombination radiation as they are not completely ionized and thus can radiate efficiently in this region. Heavy impurities can accumulate in the plasma core which leads to a significant power loss and plasma instability. Such an accumulation of heavy impurities can be avoided by ECRH heating of the core as this enhances anomalous transport processes [7].

In the SOL and in the divertor instead, the electron temperature is rather low (1 – 100 eV) and atoms are neutral or only in low ionization states. Line radiation and recombination radiation is dominating here. In standard cases, the highest

2 Plasma Radiation and Bolometry

radiation can be found in the divertor legs, close to the strike points of the separatrix with the divertor target plates. This radiation is coming from hydrogen and low ionized impurity atoms that are sputtered out of the wall material. With increasing distance from the strike points the impurity particles become further ionized. The distance of the resulting radiation from the target plates depends on the plasma gas due to the changed influx of wall impurity particles [8]. Since the plasma facing components in ASDEX Upgrade were changed from carbon to tungsten, the amount of intrinsic impurities in the plasma decreased [9]. Also radiation coming from the X-point and from a small band between the strike points and the X-point can be observed. Its origin are higher ionized impurities sputtered from the wall. In the main chamber the intrinsic radiation comes mostly from a region along the separatrix. Altogether, a fraction of 60-80% of the input heating power is dissipated by radiation in standard operation [10].

2.1.3 Cooling Factor

As seen above, different types of radiation can be observed in a tokamak plasma, the main part being line radiation. One way to treat the radiated power for different impurities is the introduction of a wavelength-independent cooling factor. The power density of radiation losses can be expressed as [11]

$$P_{rad} = \sum_Z n_e n_Z L_Z(T_e) \quad (2.3)$$

with the cooling factor $L_Z(T_e)$ for an ion species with charge Z . As $L_Z(T_e)$ and T_e are both known (examples for L_Z curves can be seen in fig. 2.1), either from theoretical calculations or from measurements, it is possible to determine the magnitude and the location of the radiation in the tokamak, combining all ionization stages of the different impurity particles.

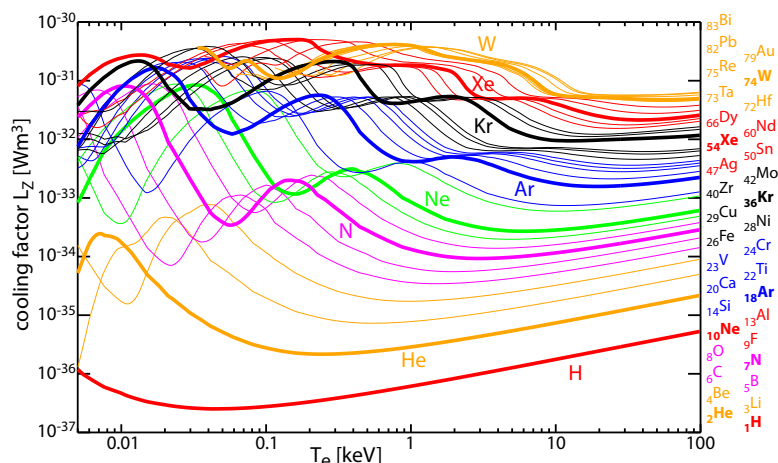


Fig. 2.1: Cooling factor for various elements. For low temperatures most elements have one or several peaks that are caused by line radiation that is dominating in this temperature range. For higher temperatures the curves are monotonously increasing due to the Bremsstrahlung that increases with $T^{1/2}$. Taken from [12].

In fig. 2.1 it can be observed that for low temperatures all atom species have one or several peaks that arise from the atomic shell structure [13]. In this temperature region the line-radiation is dominant. As the plasma is operated at electron temperatures below 10 keV (which are only reached in the core), the major fraction of measured plasma radiation is line radiation. For higher temperatures the atoms are partially or fully ionized and bremsstrahlung becomes dominant.

2.1.4 Impurity Seeding

As for future fusion devices it will be important to increase the fraction of power that is dissipated by radiation, the intrinsic radiation of the regular operation will not be sufficient. Additional radiation in the edge as well as in the confined region is necessary in order to reduce the power load onto the divertor plates. This radiation can be achieved by the deliberate seeding of impurity particles into the plasma [14]. Depending on the type of impurity, the core radiation (using e.g. krypton

2 Plasma Radiation and Bolometry

or tungsten) or the edge radiation can be increased (e.g. with argon, nitrogen or neon). At ASDEX Upgrade experiments and calculations have been performed in order to analyze the radiation characteristics of various gases in order to find a suitable impurity mixture for increasing the radiated power fraction.

The currently preferred solution scenario for ITER is the forming of a detached divertor. The detachment of a plasma is a state in which large gradients of the plasma pressure parallel to the magnetic field lines can be observed, leading to a reduction of the ion flux onto the plasma facing components [15]. The plasma power is then completely dissipated by radiation and the ions are neutralized before they can reach the divertor plates. The seeding of impurities can lead to a cold, dense region with increased radiation near to the X-point, a so-called MARFE (Multifaceted Asymmetric Radiation from the Edge) [16]. The reduced power flux on the divertor plates can lead to a detachment of the divertor [4]. Due to its low temperature, a MARFE can become unstable, leading to a disruption.

The location of the impurity radiation is important for an effective cooling that does not affect the stability of the plasma. With the knowledge of the atomic data the cooling factor L_Z can be calculated and applied onto the electron temperature distribution that can be determined by measurements. As a result, one obtains radiation patterns as in fig. 2.2.

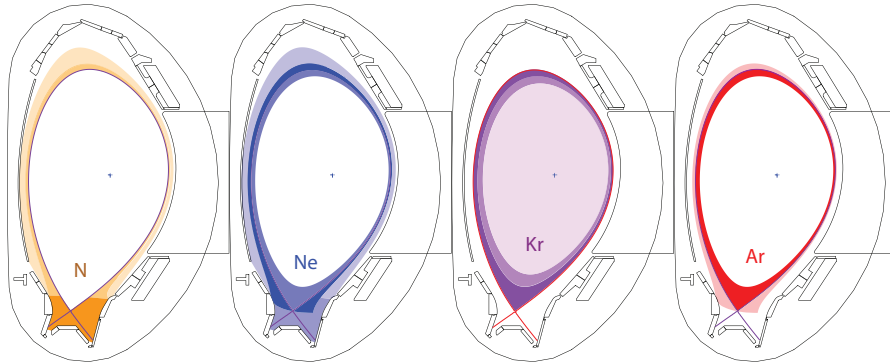


Fig. 2.2: Estimated radiation profiles, according to the specific cooling factors and the electron temperature distribution. From left to right: Nitrogen, Neon, Krypton, Argon. Images courtesy of M. Bernert, see [17].

In order to better understand and control these seeded impurities it is necessary to compare the theoretical radiation behavior with a measurement. A measured radiation profile and the total amount of radiation can be obtained by bolometry. From such measurements one can see that the actual radiation profiles differ from the theoretical predictions (see fig. 2.3). The responsible mechanisms are not fully understood yet. Though, it shows the importance of reliable measurements of the radiation with bolometers.

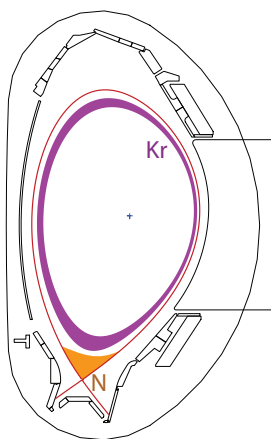


Fig. 2.3: Sketches of an actual radiation distribution for krypton and nitrogen. Image courtesy of M. Bernert, see [17].

2.2 Foil Bolometers

In ASDEX Upgrade there are two types of bolometers installed: foil bolometers and diode bolometers (using AXUV diodes [18]). In the latter, the incident radiation creates electron-hole-pairs in a semiconductor, resulting in a photocurrent proportional to the incident power which is then measured. Since this kind of bolometers cannot be calibrated absolutely [4, 19], the foil bolometer system is used to determine $P_{rad,tot}$. This is also the standard method, used in almost all fusion experiments.

2 Plasma Radiation and Bolometry

In general, fusion plasmas can be considered optically thin in the sensitivity range of a foil bolometer. (Opacity may be a problem at very high densities and low temperatures though). Therefore, the power emitted by the plasma along the line of sight of the bolometer equals the integral over the emissivity along this line of sight [20] and is called the line-integrated brightness.

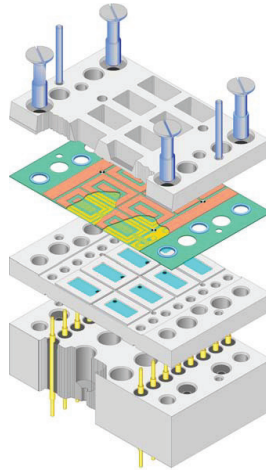


Fig. 2.4: Drawing of a bolometer head with 4 bolometer pairs. One can see the front plate, the layer with the metal foil and the substrate, the back plate, and the contacts for measuring. Taken from [19].

In a foil bolometer, the incident radiation is absorbed by a thin metallic foil (mostly gold or platinum) and converted into heat. Since the foil absorbs all incoming photon energy, this method is nearly independent from the photons' wavelength [5].

The metallic foil is placed on a substrate on whose bottom a meander structure (see fig. 2.4) is forming a resistance. By measuring the resistance change of this structure, the temperature of the foil can be deduced and the incident power can be calculated. The time resolution of such a bolometer is in the order of 2 ms, being the result of the heat diffusion through the material and other delaying effects caused by properties of the material and the electric circuits.

Usually, two bolometers are built in as a pair, where one of them is exposed to the radiation while the other is shielded from it and serves to exclude background effects, such as background temperature or pressure from the measurement. The meander resistors of both bolometers can then be arranged in a Wheatstone Bridge (see fig. 2.5).

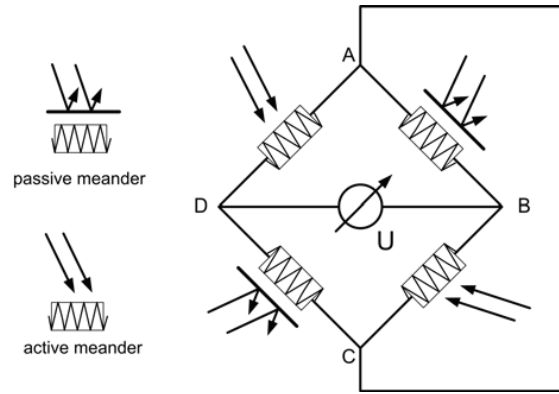


Fig. 2.5: Circuit of the Wheatstone Bridge. For a more precise measurement, two conductors are contained in each meander. One meander is covered (passive) to take into account heat and pressure effects. Voltage is applied at points A and C, the measurements of the voltage between B and D determines the resistance of the active meander. Taken from [19].

Applying a voltage to the midpoints (A,C) of the Wheatstone Bridge, one can determine the incident power by

$$P_{in} = \frac{dE_{in}}{dt} = \frac{C_1}{\tau} \cdot U + C_2 \cdot \frac{dU}{dt} \quad (2.4)$$

with U being the voltage measured between the points B and D, C_1 and C_2 constants depending on the properties of the material (such as the heat capacity) and the electric circuits. τ is the cooling time constant. These constants are determined before every shot by calibration measurements.

2 Plasma Radiation and Bolometry

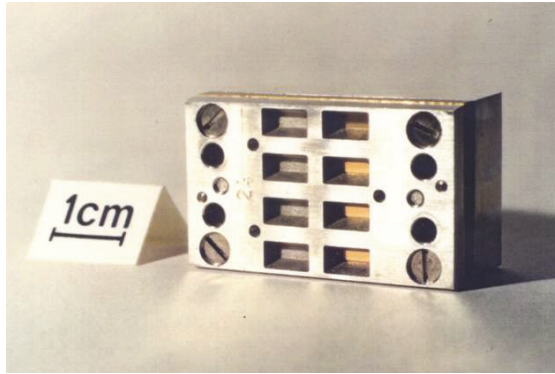


Fig. 2.6: A bolometer head with 4 open (right) and 4 covered detectors (left). Taken from [19].

The foil bolometers at ASDEX Upgrade are contained in bolometer heads with 4 bolometer pairs, see fig. 2.6. Several of these bolometer heads can be grouped behind one pinhole, resembling one camera. Several of these cameras are distributed around the poloidal cross-section of the tokamak. The horizontal camera FHC and the vertical camera FVC are each covering the complete tokamak cross-section. As in the divertor a higher resolution is necessary, the FHS camera is facing the divertor from the high field side while the FLX camera provides a horizontal view of the X-point region. The divertor legs were covered by the FDI and the FDO camera. Since the 2015 campaign, they were substituted by the FDC camera which additionally covers the X-point region. Also with the FLH camera further lines of sight into the divertor were included. In the 2015 campaign, 128 lines of sight are used to measure the plasma radiation (see fig. 2.8). As this thesis started before the new FLH and FDC cameras were built in, the proposed new $P_{rad,tot}$ algorithm is developed only using the bolometer configuration of the 2014 campaign, as it can be seen in fig. 2.7. However, the new cameras will be implemented as well.

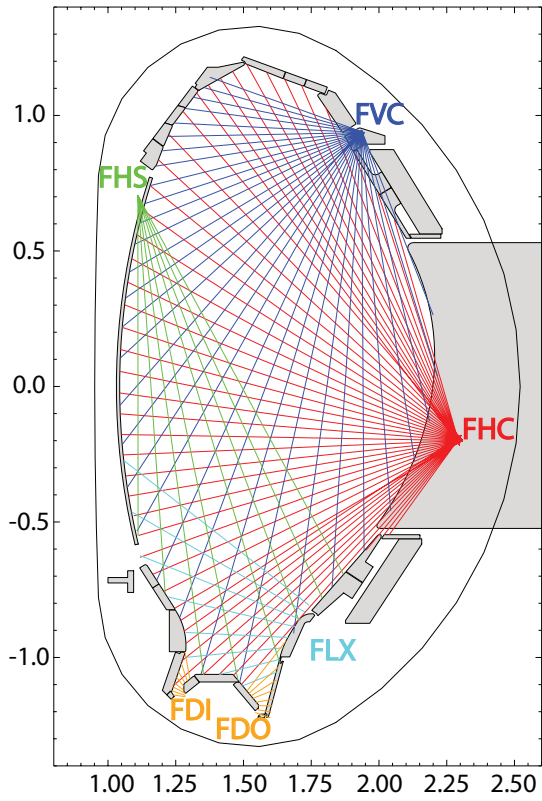


Fig. 2.7: Foil bolometer configuration in the 2014 campaign.

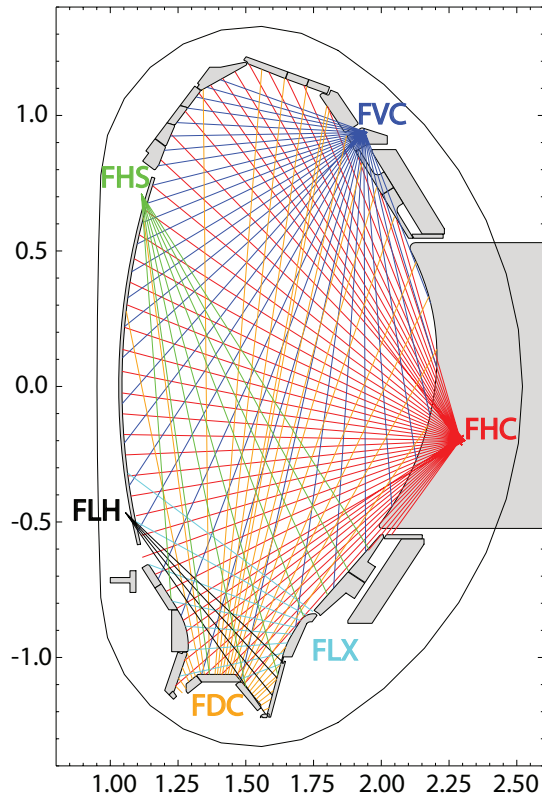


Fig. 2.8: Foil bolometer configuration in the 2015 campaign.

3 Determining the Total Radiated Power

The basic problem when measuring the plasma radiation is that the measured power deposition on the bolometers is not a localized measurement but instead the integrated values along the lines of sight. To gain the total radiated power $P_{rad,tot}$ from these measurements it is necessary to apply an algorithm on them. In this chapter, three kinds of such algorithms are presented. As all of these algorithms require knowledge of the shape of the magnetic flux surfaces, the method used at ASDEX Upgrade for their reconstruction is introduced first.

3.1 Reconstruction of the Magnetic Flux Surfaces

Many diagnostics rely on the knowledge of the shape of the magnetic field. Therefore it is crucial to reconstruct the magnetic equilibrium from measurements. The measurements of the magnetic field can be done with magnetic pick-up coils that are distributed around the plasma vessel. In order to receive a complete magnetic flux profile as shown in fig. 1.2, a reconstruction from the single measurements is necessary. Reconstruction algorithms for modeling such a profile that is in accordance with the Grad-Shafranov equation for tokamaks [21]

$$-\left(\frac{\partial^2 \Psi}{\partial R^2} - \frac{1}{R} \frac{\partial \Psi}{\partial R} + \frac{\partial^2 \Psi}{\partial z^2}\right) = \mu_0 R j_\phi \quad (3.1)$$

3 Determining the Total Radiated Power

(with Ψ being the magnetic flux and j_ϕ the toroidal current density profile) are available, but take too much calculation time for the purposes of fast diagnostic calculations. A fast way to reconstruct a magnetic flux profile (with lower temporal resolution) is the Function Parametrization (FP). First, an equilibrium code, based on the Grad-Shafranov equation, creates a database of equilibrium profiles for the complete parameter space of ASDEX Upgrade. This step has to be performed only once for each setup. The actual reconstruction is then a regression calculation that is using the measurements of the coils as input parameters. With this method, the magnetic flux profile can be reconstructed within the time between two plasma discharges.

3.2 Tomography

When attempting to gain $P_{rad,tot}$ from bolometric measurements, one can perform a tomographic reconstruction in order to get a poloidal radiation distribution and by that also the total radiated power. Several different tomographic methods can be applied which are explained in the following.

3.2.1 The Radon Transform

The measurement of a bolometer can be expressed by the Radon formula

$$f_i = \iint K_i(x, y)g(x, y)dx dy \quad (3.2)$$

where f_i denotes the measured power of the i -th line of sight, $g(x, y)$ the 2D emissivity profile in the poloidal cross-section of the tokamak and $K_i(x, y)$ the geometric correlation of measurement and emissivity profile. Assuming a straight line of sight (i.e. the beam width is not taken into account), $K_i(x, y)$ can be written as

$$K_i(x, y) = \delta(l_i + (x - x_0) \sin \theta_i - (y - y_0) \cos \theta_i) \quad (3.3)$$

(see fig. 3.1 for a graphical explanation).

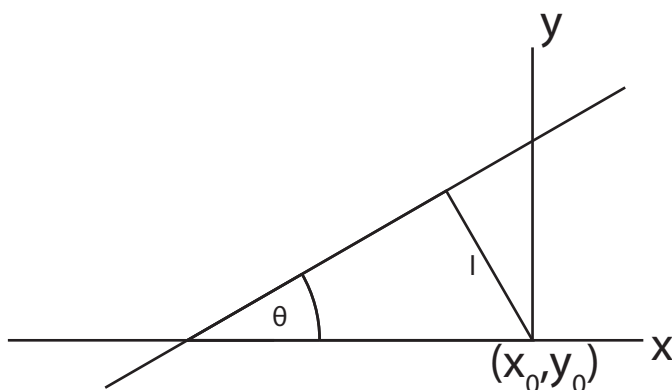


Fig. 3.1: Transform of the lines of sight's coordinates from (x, y) space into (l, θ) space. (On the basis of [22, Fig. 9a])

In mathematics, problems like the inversion of eq. (3.2) (i.e. the calculation of the emissivity profile $g(x, y)$ from measurements f) are referred to as ill-posed problems since they often lack of a unique and stable solution. There are two possible ways to treat this problem: 1. finding an analytic solution and discretization of the resulting inversion formula (called transform methods); 2. discretization of the problem and finding of a numeric solution (series expansion methods). In the following a small overview over these two approaches and their applicability in plasma tomography will be given, partly based on the introductory article of Ingesson [22] and chapter 6 of Herman's book [23]. For further reading, see also the book of Natterer [24].

3.2.2 Transform Methods

To simplify the following equations it is expedient to transform the emissivity profile $g(x, y)$ into polar coordinates $h(r, \phi)$, using the relations $x = r \cos \phi$ and

3 Determining the Total Radiated Power

$y = r \sin \phi$. Eq. (3.2) can be expressed in the form that a functional \mathcal{R} is acting on the emissivity profile $h(r, \phi)$:

$$f(l, \theta) = \mathcal{R}h(r, \phi) \quad (3.4)$$

with l and θ as defined in fig. 3.1. This transform serves mathematical purposes only and has no physical explanation. The challenge is now to find a functional \mathcal{R}^{-1} with the property $\mathcal{R}^{-1}\mathcal{R}g = g$. Such a solution can be of the form:

$$[\mathcal{R}^{-1}f(l, \theta)](r, \phi) = \frac{1}{2\pi^2} \iint \frac{1}{r \cos(\theta - \phi) - l} \frac{\partial}{\partial l} f(l, \theta) dl d\theta \quad (3.5)$$

However, in practice a reconstruction of an emissivity profile using an analytic formula is difficult to establish. In eq. (3.5) a singularity and a derivative occur which both create problems in a tomography algorithm based on this inversion formula using real data with measurement errors and a finite number of lines of sight. There are ways to use the mathematical properties of this solution, though. Since the Radon transform is related to the Fourier transform, one can use Fourier analysis to find a solution.

One method using this relation is the filtered backprojection (FBP) [25]. The projection f_i of $g(x, y)$ along K_i is transformed into the Fourier domain, multiplied by a filter function that filters out high spatial frequencies, back-transformed and then used in eq. (3.2) to determine $g(x, y)$. This method can be implemented easily and has a low calculation time. Though, this method requires a regular distribution of the lines of sight (e.g. parallel, orthogonal or fan-line), which is normally not given for bolometer systems in fusion devices.

In general, there are a lot of issues adapting analytic tomography algorithms, which are often developed and applied in medical tomography (like the FBP), for determining the distribution of radiation (or other properties) in a plasma:

1. In the inversion formulas, there are often (as in eq. (3.5)) differentials and singularities. Both tend to amplify noise and other measurement errors.
2. There is no possibility to use a priori information in analytic methods. However, this is necessary, since the number of lines of sight in a fusion device is often limited.
3. As seen above, often there are known solutions only for special line of sight geometries which are easy to realize in medical application either because there are enough detectors or by simply rotating the source and the detector. For a fusion device, this is difficult to realize due to the lack of space and the rapid change of the plasma with time.
4. Implicitly, analytic tomography algorithms contain an assumption about the uniformity of $g(x, y)$. For medical application this might be true, but not for a fusion device where strong localized radiation asymmetries can occur, e.g. in the divertor.

Analytic inversion is therefore no reliable candidate in order to calculate the emissivity distribution of a plasma.

3.2.3 Series Expansion Methods

The series expansion methods use a set of basis functions $b_j(x, y)$ to express the continuous emissivity profile $g(x, y)$ as a discrete profile

$$g(x, y) = \sum_j g_j b_j(x, y) \quad (3.6)$$

where g_j are expansion coefficients. Theoretically many kinds of functions are possible for b_j , e.g. spherical functions or functions that match the flux surfaces. But the most common approach is to assume them to be square pixels. Defining

3 Determining the Total Radiated Power

$$K_{ij} = \iint K_i(x, y) b_j(x, y) dx dy \quad (3.7)$$

eq. (3.2) can now be written as

$$f_i = \sum_j K_{ij} g_j \quad (3.8)$$

which corresponds to the matrix equation

$$f = Kg \quad (3.9)$$

Basically, this equation could be solved by finding the matrix K^{-1} . This would require K to be an invertible matrix which is rarely the case. Often the number of lines of sight is much smaller than the number of pixels, making K a non-square matrix and therefore not invertible. To solve such an underdetermined system anyway, a regularization is necessary, which means the inclusion of more information about the expected emissivity distribution.

3.2.4 Constrained Optimization

One way to give such kind of a priori information to the tomography is the constrained optimization. The constrain function $C(g)$ is given by the measurements. For those the following inequation is valid:

$$\frac{1}{I} \sum_{i=1}^I \frac{(f_{i,calc}(g) - f_i)^2}{(\epsilon_i f_i)^2} \leq 1 \quad (3.10)$$

which can be written as

$$C(g) = \frac{1}{I} \sum_{i=1}^I \frac{(f_{i,calc}(g) - f_i)^2}{(\epsilon_i f_i)^2} - 1 \leq 0 \quad (3.11)$$

The actual measurement values are denoted as f_i , the values back calculated from the solution as $f_{i,calc}$. ϵ_i is a relative error parameter that can be chosen for each line of sight for taking into account noise, non-optimal calibration of the bolometers, errors from the measurements averaging over time etc.

The objective function $O(g)$ contains information about the expected properties (e.g. smoothness) of the emissivity profile $g(x, y)$. We will set a specific function for $O(g)$ later in sec. 3.2.5. If $O(g)$ is of the form [26]

$$O(g) = \int \left(\hat{H}(g) \right)^2 dx dy \quad (3.12)$$

($\hat{H}(g)$ is a linear homogeneous operator), the Lagrange multiplier method can be used for the minimization

$$\min \{O(g) \mid C(g) \leq 0\} \quad (3.13)$$

of the objective function $O(g)$ under the constrain function $C(g)$. Expression 3.13 can then be written as

$$\min \{O(g) + \lambda C(g)\} \quad (3.14)$$

where λ is the Lagrange multiplier. The influence of the objective and the constrain function depends now on λ . With a small λ , information from the objective function will dominate the solution. The resulting profile g will match the expected properties but be in low accordance with the measurement values f . On the other hand, for big λ the measurements will dominate, neglecting the desired profile

3 Determining the Total Radiated Power

properties. The best value for λ can be found by demanding the constrain function (3.11) to be true (also called the discrepancy principle; see also fig. 3.2 for a graphical representation):

$$C(g) = \frac{1}{I} \sum_{i=1}^I \frac{(f_{i,calc}(g) - f_i)^2}{(\epsilon_i f_i)^2} - 1 = 0 \quad (3.15)$$

It can be proven that for this case the solution is existing and unique if the assumed relative errors $\epsilon < 1$. The optimal λ can be found by iteration.

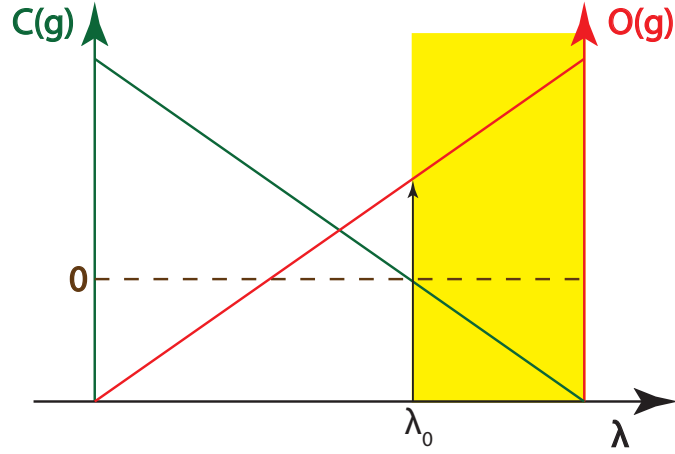


Fig. 3.2: Graphical representation of the discrepancy principle. For small λ , the objective function $O(g(\lambda))$ will dominate, for high λ the constrain fuction $C(g(\lambda))$. For $\lambda > \lambda_0$ (yellow area) the constrain function (3.11) is true. For $\lambda = \lambda_0$, the objective function $O(g(\lambda))$ is minimal and an unique solution exists. (On the basis of [22, Fig. 14] and [26, Fig. 4.1]).

3.2.5 Anisotropic Diffusion Model Tomography

At ASDEX Upgrade the Anisotropic Diffusion Model Tomography (ADMT) is used that was developed by Fuchs [27]. It is based on the constrained optimization that was introduced above. The minimization of radiation sources and sinks serves as the

objective function. To gain the objective function it is assumed that the variation of the radiation varies less along the magnetic flux surfaces than perpendicular to them. This is similar to the transport of plasma particles. However, it should be emphasized that this radiation diffusion is only a model without any directly underlying actual physical processes. One can formulate a diffusion equation, though:

$$\operatorname{div}(D \operatorname{grad} g) = -s + \frac{\partial g}{\partial t} \quad (3.16)$$

D denotes here the anisotropic diffusion tensor and s the sum of the emissivity sources and sinks. The left hand side of eq. (3.16) can also be written as

$$\operatorname{div}(D \operatorname{grad} g) = \operatorname{div}(n D_{\perp} n \cdot \nabla g + t D_{\parallel} t \cdot \nabla g) \quad (3.17)$$

where n and t are the normal and the tangential vectors with respect to the flux surfaces. $D_{\perp}(R, z)$ and $D_{\parallel}(R, z)$ are the perpendicular and the parallel diffusion parameters in cylindrical coordinates. To find a solution that minimizes sources and sinks of radiation, the following equation has to be fulfilled:

$$\min = \int (\operatorname{div}(D \operatorname{grad} g)) \, dR dz + \lambda \sum_{i=1}^I \frac{(f_{i,calc}(g) - f_i)^2}{(\epsilon_i f_i)^2} \quad (3.18)$$

The optimal λ can then be found by iteration [28].

The diffusion parameters $D_{\perp}(R, z)$ and $D_{\parallel}(R, z)$ can be set for the different regions of the tokamak cross-section (see fig. 3.3). The spatial dependence of the diffusion parameters takes into account that in the confined region the particle transport along the magnetic flux surfaces is higher than the transport perpendicular to them, whilst in the divertor region perpendicular transport is increased. For the

3 Determining the Total Radiated Power

radiation, one can expect a similar behavior. A typical result of the ADMT can be seen in fig. 3.4.

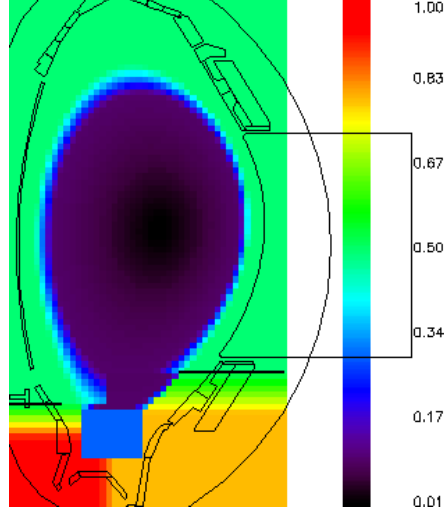


Fig. 3.3: Example for the spatial dependence of the ratio D_{\perp}/D_{\parallel} of the diffusion parameters. In the core (black) it is the lowest, increasing towards the separatrix (blue) and the SOL (green). In the divertor region one can see the X-point region (blue square) and the inner (red) and the outer divertor (yellow) with high perpendicular radiation diffusion.

Although the ADMT gives good results and one could determine the total radiated power from it (using eq. (3.26)), the algorithm is very time consuming due to the usually great number of pixels which is necessary in order to have a sufficient resolution. Calculating the time trace for one discharge would take hours. This result wouldn't even be very trustworthy since it requires some experience to determine the right diffusion parameters for each point in time. For the determination of $P_{rad,tot}$ a faster method is necessary.

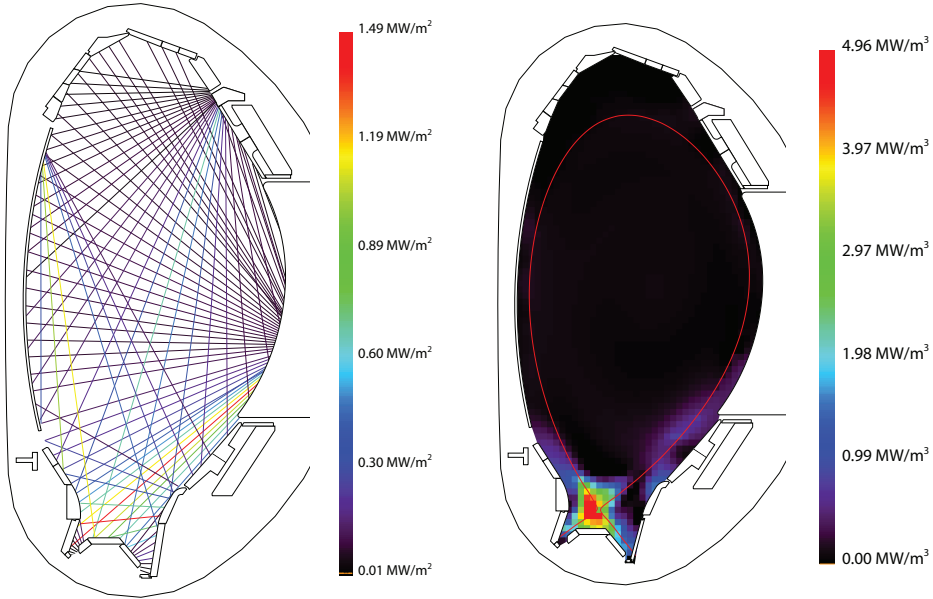


Fig. 3.4: Foil bolometer measurements for AUG shot 30410, 4.00 s (left) and the radiation profile reconstructed from these measurements with ADMT (right).

3.3 The BPD Algorithm

As the results for $P_{rad,tot}$ are widely used at ASDEX Upgrade, it is reasonable to automatize its calculation. For this, assumptions such as the additional input parameters for the tomography have to be avoided. One way to do this is to process the measurement data of one single camera that covers the whole plasma cross-section.

The radiation power can be expressed as

$$P_{rad,tot} = \int_V \epsilon \, dV = 2\pi \int_{R_M - a_{max}}^{R_M + a_{max}} \int_{z_u}^{z_o} u \, dz \, R \, dR \quad (3.19)$$

3 Determining the Total Radiated Power

with ϵ being the space-dependent emissivity, V the plasma volume, R_M the major plasma radius and a_{max} the minor plasma radius. z_o and z_u are the upper and the lower boundaries in z-direction.

The BPD algorithm (with BPD standing for **B**olometric **P** R_{RAD}) [28] uses the magnetic equilibrium (see sec. 3.1) to assign each line of sight of the FVC camera the magnetic flux surface that is contacted tangentially by the line of sight. The basic assumptions of the BPD algorithm are that these flux surfaces are concentric ellipses and that the area between such flux surfaces has a constant emissivity. From the magnetic equilibrium, the minor axis a and the eccentricity k of the ellipses can be determined. With a coordinate transform, the ellipses can be represented as circles. As the emissivity within an area between two flux surfaces is constant, a rotation of the line of sight around the inner flux surface does not change the integral along this line of sight. Therefore, the line of sight can be rotated around the inner of the two flux surfaces until it is vertically orientated.

The integral along the line of sight can now be written as

$$J = \int_{\tilde{z}_u}^{\tilde{z}_o} u(a) d\tilde{z} \quad (3.20)$$

which is the second integral in eq. (3.19). Also, the integral along a line of sight is the measured line-integrated brightness (see eq. (3.2)). $P_{rad,tot}$ can then be calculated by discretizing eq. (3.19):

$$P_{rad,tot} = 2\pi k \sum_{i=1}^I \tilde{J}_i R_i \delta a_i \quad (3.21)$$

with i denoting the lines of sight, \tilde{J}_i the measured line-integrated brightness of the i -th line of sight, R_i the major plasma radius of the rotated i -th line of sight and δa_i the width of the constant emissivity area that is defined by this line of sight.

At ASDEX Upgrade this algorithm is in use for many years and was also tested and benchmarked when it was introduced. After recent improvements on the bolometer system in order to minimize reflections inside the camera, the measured powers turned out to be lower than before [29]. As a result, the radiated power fraction calculated with the BPD algorithm was too low compared to the fraction calculated with the tomography. This implies that the BPD algorithm might be less accurate than expected and a new algorithm for the calculation of $P_{rad,tot}$ is necessary. In the following, as part of this master thesis, a new algorithm based on an Abel inversion was implemented and benchmarked against the existing BPD algorithm and the tomography.

3.4 Abel Inversion Based Algorithm

3.4.1 Abel Inversion

In order to perform an Abel inversion, a poloidally symmetric plasma is assumed. Considering the small variations of many plasma characteristics along the magnetic flux surfaces compared to their perpendicular variations, this assumption is true for a tokamak up to a certain degree. Let us assume that a two-dimensional circular plasma with radius R has the circular symmetric emissivity distribution $f(r)$ (with $r = \sqrt{x^2 + y^2}$; see fig. 3.5). Infinite parallel lines of sight crossing the half of the plasma create a one-dimensional projection function $F(y)$. This projection function can be expressed and simply mathematically transformed as follows:

$$F(y) = \int_{-\infty}^{+\infty} f(\sqrt{x^2 + y^2}) dx = 2 \int_0^{x_r} f(r(x)) dx = 2 \int_y^R f(r) \frac{r}{\sqrt{r^2 - y^2}} dr \quad (3.22)$$

To obtain $f(r)$ back from $F(y)$, there is an analytic solution for eq. (3.22):

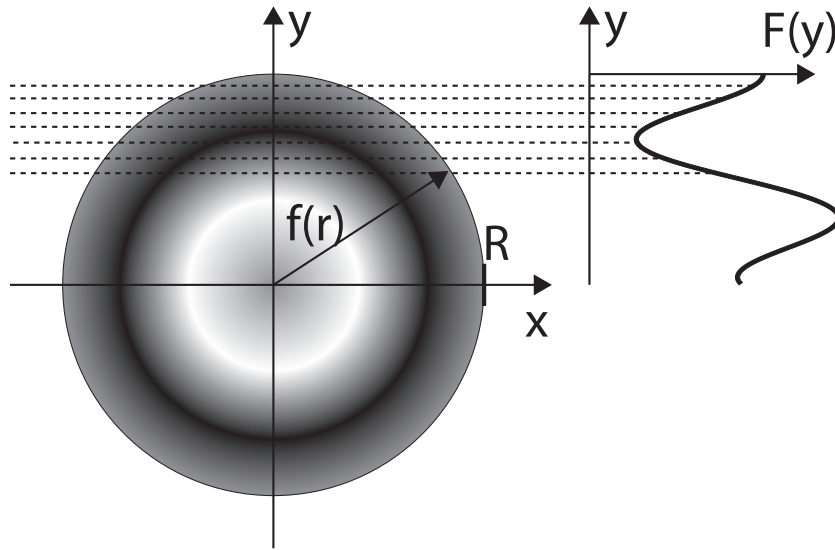


Fig. 3.5: Abel transform: parallel lines of sight create a projection function $F(y)$ from a circular symmetric distribution function $f(r)$.

$$f(r) = -\frac{1}{\pi} \int_r^R \frac{dF(y)}{dy} \frac{dy}{\sqrt{y^2 - r^2}} \quad (3.23)$$

For various reasons, this equation cannot be applied directly on our problem. As in the discussion of tomography methods above (see sec. 3.2.2), a differential occurs in the equation, making the solution susceptible for measurement errors. Also, it assumes an infinite density of measurements and a certain geometry which cannot be provided under the conditions of a nuclear fusion device.

3.4.2 Slice-and-Stack Method

Nevertheless, one can use a numerical implementation of the Abel inversion instead, called the slice-and-stack method [30]. Its basic assumption is that the plasma forms zones of constant emissivities ϵ_i , each traversed by exactly one line of sight that is measuring the power P_j (see fig. 3.6). Given the lengths $L_{j,k}$ that the

3.4 Abel Inversion Based Algorithm

j -th line of sight travels through the k -th zone, the emissivity of each zone can be determined by subtracting the contributions of the more outer shells:

$$\epsilon_k = \frac{P_k}{L_{k,k}} - \sum_{j=1}^{k-1} \epsilon_j \frac{L_{k,j}}{L_{k,k}} \quad (3.24)$$

The advantage of this method is that it is also applicable on non-circular symmetries (as given by the flux surfaces).

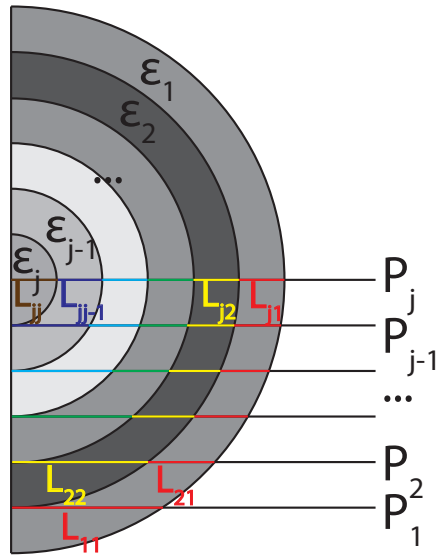


Fig. 3.6: The principle of the slice-and-stack method: the layers of constant emissivity ϵ_j are traversed by an equal number of lines of sight. Each line of sight P_j traverses one more layer than its neighbor P_{j-1} to the outside. With the lengths $L_{j,k}$ known, it is possible to determine the emissivities.

3.4.3 Implementation at ASDEX Upgrade

To implement the slice-and-stack method, the FHC camera lines (see fig. 2.7) above the magnetic axis are used. They have a high radial coverage and are not facing into the divertor. The latter is important as the highly asymmetric divertor

3 Determining the Total Radiated Power

radiation would violate the assumption of constant emissivity within the radiating layers. For this reason, the Abel inversion will only be applied to the main chamber plasma. The divertor will be treated differently, see sec. 3.4.5.

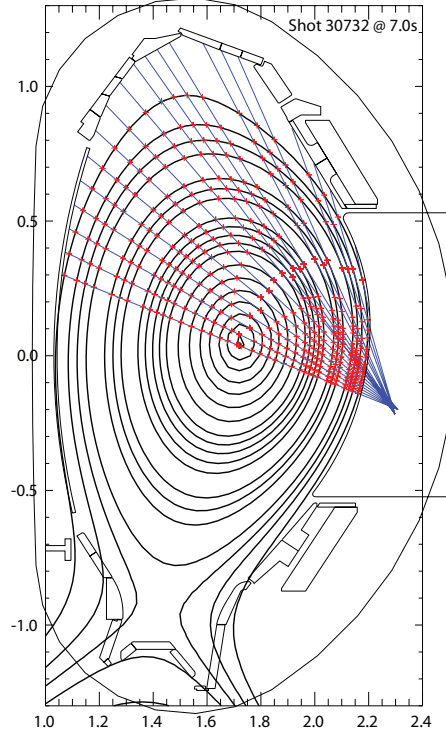


Fig. 3.7: Intersection points of the FHC camera's lines of sight and the magnetic flux surfaces.

Those layers are defined by the lines of sight (see fig. 3.7) and the lengths $L_{j,k}$ of each line of sight through each layer can be calculated.

Knowing also the powers measured by those lines of sight, one can apply the Abel inversion algorithm according to eq. (3.24). The result will look like in fig. 3.8, but it can also be depicted as a profile of ρ_{pol} (see fig. 3.9). Also negative emissivity values are possible, even though they are not physically correct. This is a result from measurement errors and asymmetries in the radiation.

3.4 Abel Inversion Based Algorithm

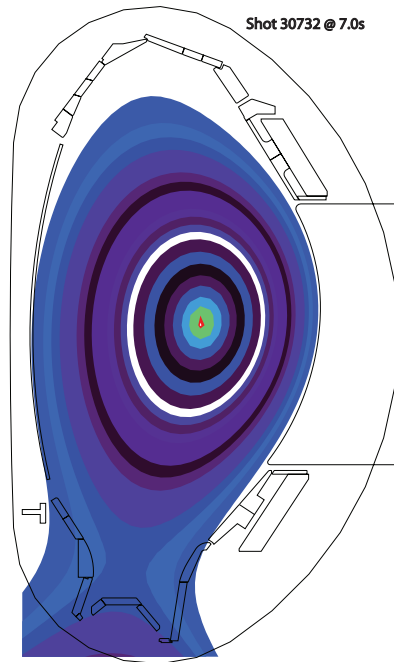


Fig. 3.8: Resulting emissivity distribution for AUG shot 30732, 7.0s. The lowest emissivity is in the black and purple areas, the highest in the yellow, orange and red areas. White color inside the separatrix indicates areas with negative emissivities.

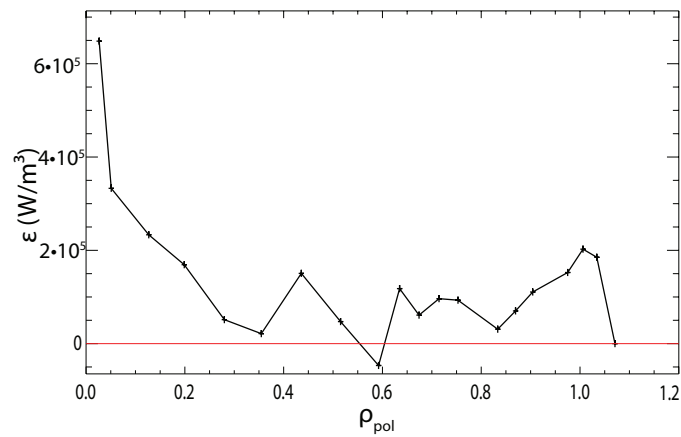


Fig. 3.9: Emissivity profile of the Abel inversion of AUG shot 30732, 7.0s. The curve shows the same data as fig.3.8. On the x-axis the ρ_{pol} of the constant emissivity areas is plotted, on the y-axis their emissivity.

3 Determining the Total Radiated Power

$P_{rad,tot}$ can now be calculated from the emissivity ϵ_j and the volume V_j of each flux region

$$P_{rad} = \int_V \epsilon \, dV = \sum_j V_j \epsilon_j \quad (3.25)$$

For regions outside the separatrix the volume is not defined and the second Guldinus theorem is used for the determination of several sub-volumes:

$$P_{rad} = \sum_i A_i \cdot 2\pi R_{bc,i} \cdot \epsilon_i \quad (3.26)$$

where A_i is the area of an arbitrary surface in the poloidal cross-section of a cylinder, $R_{bc,i}$ the major radius of its barycenter and ϵ_i its emissivity that is assumed to be constant over all the surface.

3.4.4 Corrections in the SOL

For the implementation of the Abel inversion only the lines of sight in the upper half of the main chamber (above the magnetic axis) were used. One could also take the lines of sight in the lower main chamber (below the magnetic axis but not facing into the divertor, see fig. 3.10) into account. To consider this, the measured line-integrated brightness of those lines of sight can be compared with the values that they are supposed to have according to the Abel inversion. It is observed that the measured values in the lower main chamber increase towards the divertor. Using them for the Abel inversion would therefore lead to significant errors in the results due to the big differences between neighboring lines of sight with a similar ρ_{pol} .

However, the values in the lower main chamber are still in the same order of magnitude as in the upper half and the excess power on the lower lines with respect

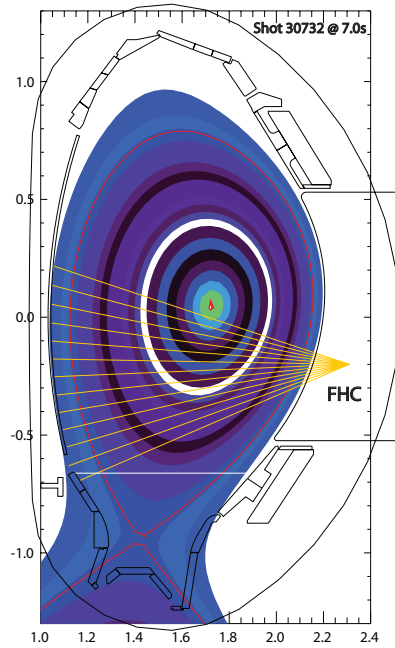


Fig. 3.10: The lines of sight of the FHC camera below the magnetic axis that are not facing the divertor. On these lines of sight higher line-integrated brightnesses are measured the closer they come to the divertor.

to the Abel inversion can be placed in the high field side SOL. From an empirical point of view, this is legit as in this region one can often observe radiation that is getting stronger towards the divertor. The observation of high field side high density regions (HFSD) [31] points also to a higher radiation in this region. However, due to the role of the major radius in eq. (3.26), the error on this excess power is maximum 2, no matter where along the lines of sight it was actually located.

In order to place the excess power, the high field side SOL was covered with small surface areas on that the excess power of the corresponding lines of sight is equally distributed (see fig. 3.11). One can see, how the values of the lines of sight increase towards the divertor. If one line of sight is deactivated, the emissivity value is estimated as the mean value of the neighboring areas. The SOL region in the upper main chamber is covered with small surface areas as well (see fig. 3.11) and

3 Determining the Total Radiated Power

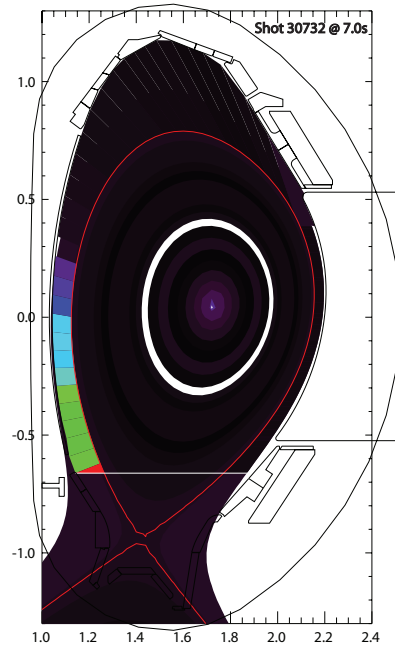


Fig. 3.11: Correction of the higher line-integrated brightnesses that are observed the closer the lines of sight come to the divertor. Excess power is placed into the high field side SOL. The color scale differs from the figures above since it is orientated at the highest emissivities which can now be found in the high field side SOL.

assigned the weighted mean emissivity values of the underlying flux zones from the Abel inversion.

3.4.5 Approach for the Divertor

In the above described method, the divertor was always excluded. It is defined by an horizontal line at $z \approx -0.66$ m. Some of the closed flux zones lay partially below this line. Since the closed flux zones were already included above with their complete volume, one has now to subtract the contribution from below the divertor separation line (using eq. (3.26)). This can be seen in fig. 3.12 as white area.

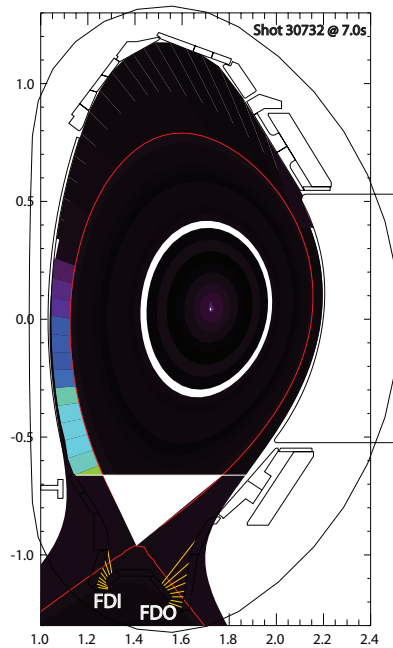


Fig. 3.12: In the divertor legs, the FDI and the FDO cameras are used to determine the local emissivity distribution. The white area's power contribution has to be subtracted from the Abel inversion in order to separate divertor and main chamber.

For the divertor a similar approach can be used as in the high field side SOL: choosing some lines of sight that are facing into the divertor, subtracting the power contribution of the Abel inversion from the lines of sight's measured values and distributing the excess power into the areas of the divertor that are covered by those lines of sight.

For the divertor legs, this procedure is straightforward. The only cameras having lines of sight in this region are the FDO and the FDI cameras (see fig. 3.12). They are not traversing the main chamber and the region of the Abel inversion. One can therefore distribute their measured power equally over the area they cover (see fig. 3.13).

For the rest of the divertor area there are 3 cameras to choose from; they all cover the remaining part of the divertor: FVC, FHS and FLX camera. The contributions

3 Determining the Total Radiated Power

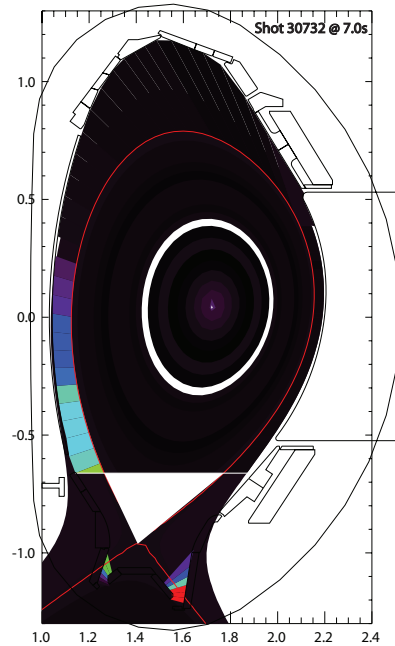


Fig. 3.13: The emissivities in the divertor legs, determined by equally distributing the line-integrated brightness of the FDI and FDO camera's lines of sight over the areas they cover.

from the Abel inversion are subtracted and the excess power distributed over the divertor. The graphical results can be seen in the figures 3.14 (FVC), 3.15 (FHS) and 3.16 (FLX). Again, in case of missing lines of sight, the emissivity values of a region was set to the mean value of their neighbors.

It is to note that only the contributions of the Abel inversion are subtracted but not those from the corrections in the SOL. Especially for the FHS this leads to errors in the results when using the FHS for the divertor.

FHS and FVC look vertically into the divertor. This means that for those cameras it is not important where along the lines of sight the power is actually originated since the major radius along those lines remains nearly constant. For the FLX camera instead, which is horizontally orientated, the difference can be a factor of 2 in the major radius, changing also the value of P_{rad} . In the following three scenarios will be treated when using the FLX camera: all the radiation comes from

Determination of the divertor radiation by using the...

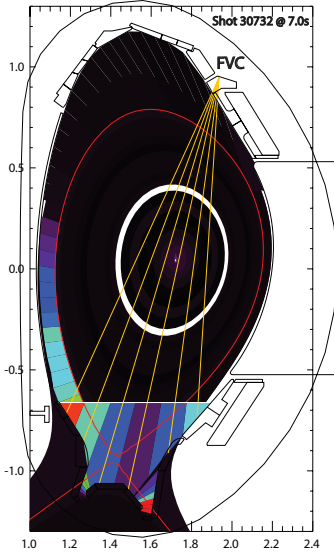


Fig. 3.14: FVC

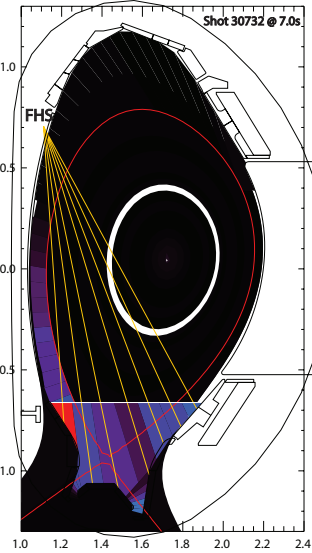


Fig. 3.15: FHS

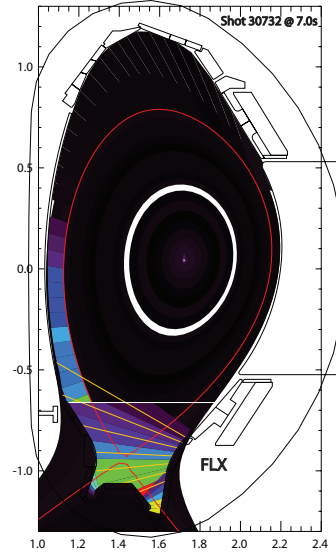


Fig. 3.16: FLX

the barycenter of each area (called FLX^* or $FLX0$), all the radiation comes from the very inner (FLX^-) or the very outer (FLX^+) point of each area.

3.4.6 Further Development

For the moment, the Abel inversion based algorithm is only able to be run on shots from the 2014 ASDEX Upgrade campaign as with the beginning of the 2015 campaign the FDI and the FDO camera were substituted by a new camera, called FDC (see sec. 2.2). The implementation of that camera into the code would also allow to have another alternative to calculate the radiation coming from the divertor.

Up to now, only lower single null scenarios can be evaluated as the algorithm assumes a certain geometry which is not given for the upper single null, double null or limiter case. As the algorithm is supposed to calculate the $P_{rad,tot}$ at ASDEX

3 Determining the Total Radiated Power

Upgrade one day, it is indispensable to include these cases and eventually a method to distinguish the respective magnetic configuration.

As the algorithm is based on several, empirically motivated assumptions, the accuracy of the whole algorithm including the Abel inversion and the corrections for SOL and divertor cannot be predicted. In order to benchmark the new algorithm, determine its accuracy, and compare it with the tomography, synthetic emissivity profiles had to be used.

4 Benchmarking and Application

The determination of the different algorithm's performance requires synthetic emissivity profiles. From those profiles the measured values of the lines of sight are back-calculated and given to the algorithms. Their result for $P_{rad,tot}$ is then compared with the known value from the synthetic profile. Evaluation of single profiles as well as statistical results will be shown in this chapter. Finally, some time traces calculated with the new Abel inversion based algorithm will be presented.

4.1 Synthetic Emissivity Profile Program

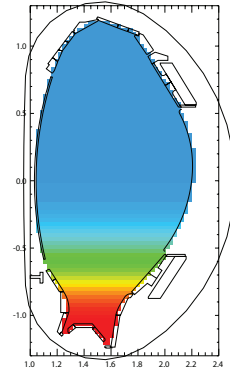
In order to create and evaluate synthetic emissivity profiles, a new program was developed. This section will give an introduction in the functioning of this program. A detailed manual can be found in appendix C of this thesis.

4.1.1 Creation of the Profiles

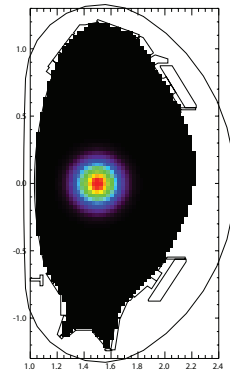
First, synthetic emissivity profiles have to be created. For this, the poloidal cross-section of the tokamak is divided into 46×84 pixels. For the creation of the emissivity profile, 6 basic emissivity scenarios can be combined:

4 Benchmarking and Application

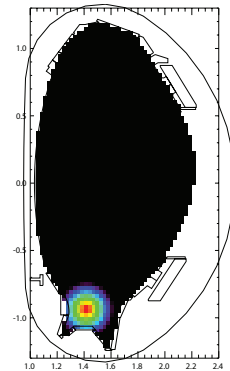
Background: Creates an uniform radiation in the background, which is also distinguishable by divertor or main chamber. To avoid the “step” that can occur between these two regions, a smoothing command is included.



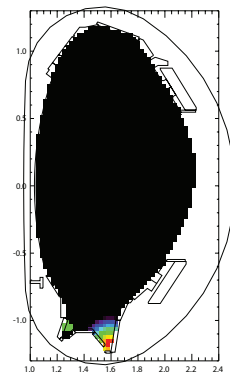
Point: Creates a point-like emissivity distribution. The position of the point, its decay with increasing distance from the center (Gaussian, Heaviside, linear, exponential) and size can be chosen.



X-Point: Applies the radiating point at the position of the X-point which is determined from the magnetic equilibrium.

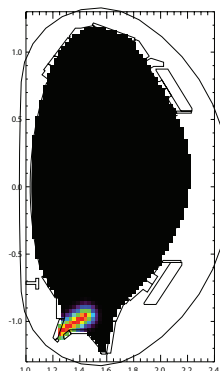


Strike Points: Applies radiating points at the position of the strike points which are calculated from the separatrix data received from the magnetic equilibrium and the vessel contour line. It is possible to apply the command on both or only one side.

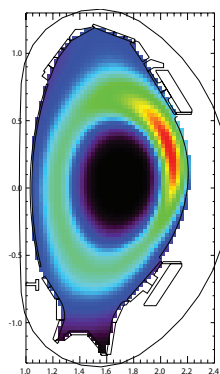


4.1 Synthetic Emissivity Profile Program

Divertor Legs: Puts radiation on a straight line between the strike points and the X-point (which are respectively determined as described above). Shape (decay) and width can be chosen. It is possible to apply the command on both or only one side.



Ring: Creates radiation in a ring that is orientated along the magnetic flux surfaces. Shape (decay), thickness and ρ_{pol} position can be chosen. Additionally, poloidal asymmetries can be placed on the ring. The angular size and the thickness of the asymmetry can be chosen, the shape is taken from the main ring. It is also possible to create only an asymmetry without an underlying ring.



The profiles are commutative, one scenario can be used several times. They are all added up to one profile. Additionally smoothing, random noise etc. can be applied afterwards.

4.1.2 Calculation of the Lines of Sight Measurements

As a second step, the measurements of the lines of sight are calculated from the created emissivity profile. To do this, the lines of sight are subdivided into smaller equidistant parts. For the calculation of the radiation along these subsections, two methods can be chosen:

- Calculating the length that each line of sight travels through each pixel area (see fig. 4.1). This length is calculated by determining the pixel in which the midpoint of one subsection is located. The line-integrated brightness of a

4 Benchmarking and Application

single subsection is then equal to its length multiplied with the emissivity of the pixel. The total line-integrated brightness of one line of sight can be determined by summing up the contributions of its subsections.

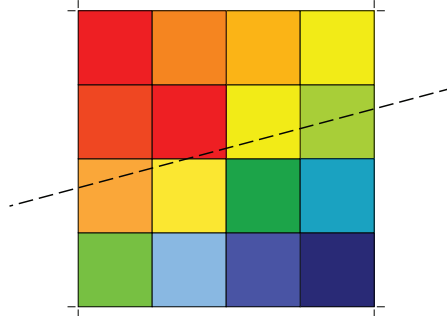


Fig. 4.1: Pixel-based back-calculation of the lines of sight

- Assigning each subsection the mean weighted emissivity of the 4 pixels that are nearest to the subsection's midpoint (see fig. 4.2). The weights depend on the distance from the pixels midpoint to the subsections midpoint. Different functions (Gaussian, Heaviside, linear, exponential) can be chosen to determine these weights. The line-integrated brightness of a single subsection is then equal to its length multiplied with the weighted emissivity of the 4 nearest pixels. The total line-integrated brightness of one line of sight can be determined by summing up the contributions of its subsections.

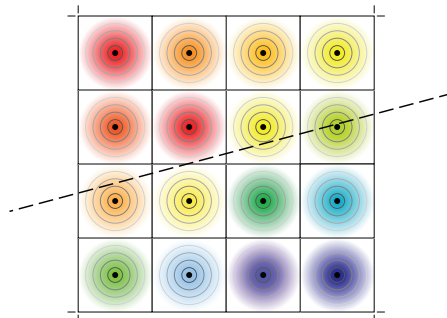


Fig. 4.2: Weight-function-based back-calculation of the lines of sight

In practice both methods are nearly equal; the second is to prefer with respect to the calculation time. Fig. 4.4 shows the result of the calculation of the lines of sight from a synthetic radiation profile (shown in fig. 4.3).

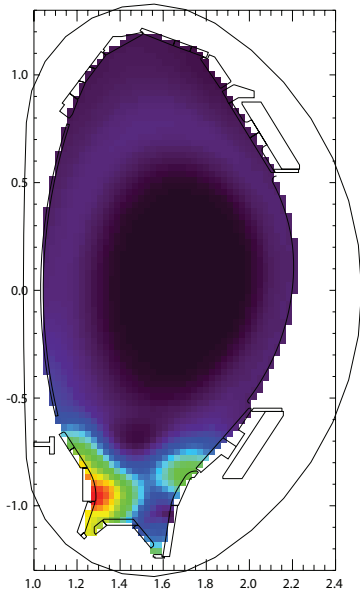


Fig. 4.3: Radiation profile

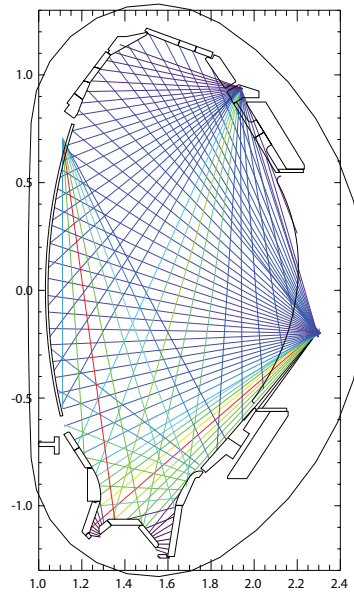


Fig. 4.4: Line of sight profile

4.2 Evaluation of Several Synthetic Emissivity Profiles

With the synthetic emissivity profile program a set of 93 profiles (see appendix B) was created and evaluated. Some insights can already be obtained from looking at single profiles. For a more reliable statement about the algorithm's accuracy a statistical evaluation is necessary, though.

The following algorithms were tested:

- The current algorithm used at ASDEX Upgrade to determine $P_{rad,tot}$, called BPD (see sec. 3.3).
- The new Abel inversion-based algorithm (see sec. 3.4). All 5 camera configurations were tested (using FVC, FHS, FLX-, FLX* or FLX+ for the calculation of the divertor).

4 Benchmarking and Application

- For comparison and benchmarking reasons also the tomography was tested automatized, using the standard, non-optimized input parameters and settings (see sec. 3.2.5).

For each profile, an exactness coefficient can be calculated:

$$E = \frac{P_{rad,tot,alg}}{P_{rad,tot,syn}} \quad (4.1)$$

with $P_{rad,tot,alg}$ is the value of the total radiated power from the examined algorithm and $P_{rad,tot,syn}$ the exact value from the synthetic profile.

4.2.1 Evaluation of Single Profiles

From the analysis of single emissivity profiles and their exactness under the different algorithms, insights in the way they work and possible improvements can be received.

Looking at the profile *010* (see fig. 4.5), one can see that the BPD algorithm's exactness is very close to the desired value of 1.000. The Abel inversion based algorithm (in the following figures abbreviated as AIBA) shows results that are not as accurate as the BPD algorithm but still within an acceptable margin of deviation. Only when using the FHS camera for the divertor area, the values are significantly too high, but this behavior was already expected from earlier observations (see sec. 3.4.5). It can be observed that the value for the FVC camera is too high while the ones for the FLX camera are all too low. As the camera lines of the FVC pass mostly through the area that is covered by the Abel inversion while the FLX lines of sight do not, the source of error must be an imprecision of the Abel inversion. Calculating the mean value from the results using FVC and FLX* could be a possible solution to compensate such kind of effects. However, further tests are necessary to confirm the utility of this approach. The result of the tomography is also acceptable but a bit too low.

4.2 Evaluation of Several Synthetic Emissivity Profiles

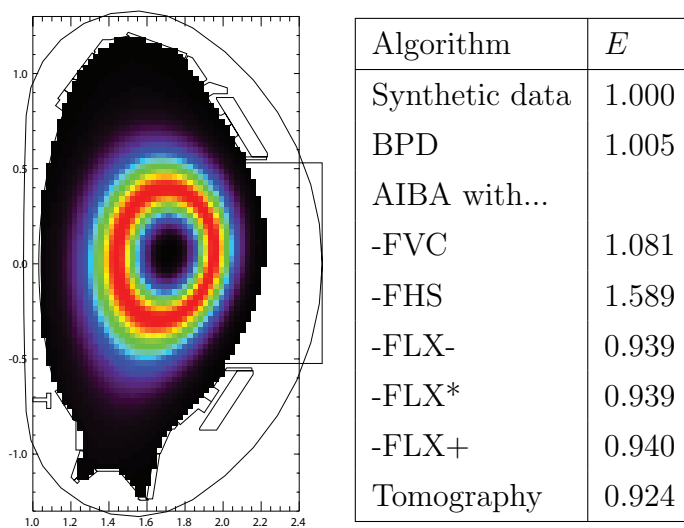


Fig. 4.5: Emissivity profile (left) and exactness parameters (right) for synthetic profile *010*.

For profile *028* (see fig. 4.6), the exactness coefficients for the Abel inversion based algorithm (except FHS) and for the tomography are sufficiently close to 1.000. The $P_{rad,tot}$ calculated by the BPD algorithm is around 30% too low, though.

The same effect can be observed in profile *031* (see fig. 4.6). Also here, the BPD algorithm's exactness is about 25% too low. But also the Abel inversion based algorithm's exactness (again except FHS) has decreased. Due to the position of the asymmetry in the upper half of the main chamber, its radiation power is assumed by the Abel inversion to come from the plasma core where it occupies a smaller volume. The algorithm is not able to compensate this effect in the divertor area with the FVC or the FLX cameras. The FVC lines of sight are directly traversing the plasma core (where no radiation is supposed to be) and the calculated radiation coming from the divertor is even lower than it should be.

Profile *093* was created on the basis of a real radiation distribution received from the tomography. The BPD algorithm's result is too low due to the radiation coming from the divertor. But also the Abel inversion based algorithm can only reproduce the radiation power within an deviation margin of 15% (except FHS). Yet, no explanation for this behavior has been found. Even the tomography's exactness

4 Benchmarking and Application

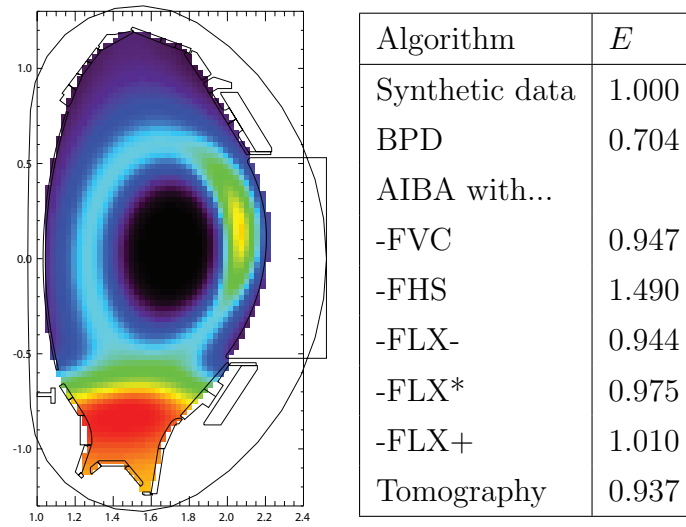


Fig. 4.6: Emissivity profile (left) and exactness parameters (right) for synthetic profile *028*.

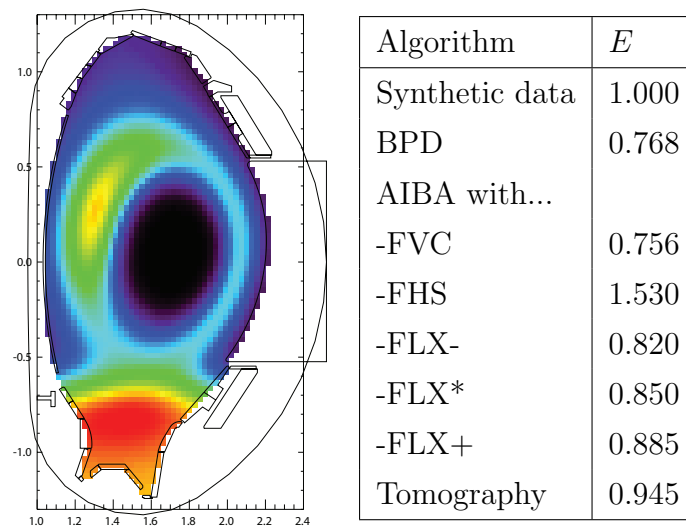


Fig. 4.7: Emissivity profile (left) and exactness parameters (right) for synthetic profile *031*.

4.2 Evaluation of Several Synthetic Emissivity Profiles

coefficient is about 10% too low. In the following subsection, a similar effect can also be observed for a statistical evaluation.

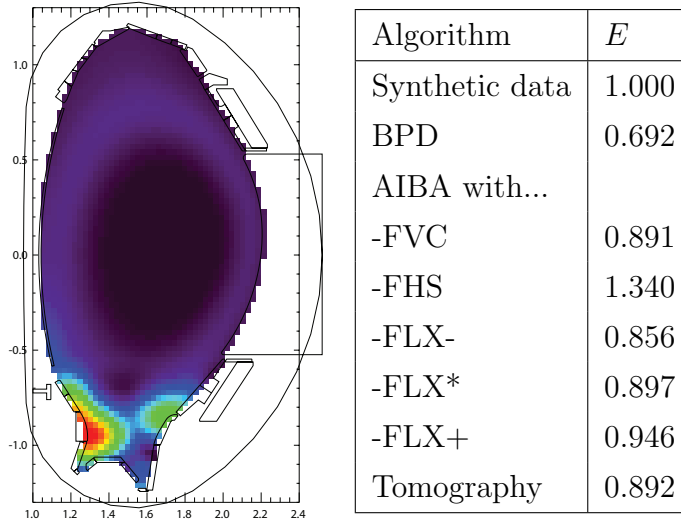


Fig. 4.8: Emissivity profile (left) and exactness parameters (right) for synthetic profile 093.

4.2.2 Statistical Evaluation

For a more reliable statement about the algorithms' accuracy a statistical evaluation is necessary. The mean value \bar{E} of all 93 scenarios can be calculated in order to compare the accuracy of the tested algorithms. Since the used scenarios are not equally realistic to occur in a tokamak plasma, they were weighted in order to calculate their mean value [32]. The scenarios and their weights can be found in appendix B. The weights were chosen by the relevance of a scenario in a tokamak plasma. The highest weights were given to scenarios that are similar to a standard discharge as described in sec. 2.1.2 and to such scenarios that can be achieved by impurity seeding (see sec. 2.1.4) and by known processes (e.g. transport, instabilities). The choice of the scenarios and their weights has an influence on the results of the statistical evaluations. An over-representation or an over-weighting of unrealistic scenarios can lead to incorrect statements about the algorithms'

4 Benchmarking and Application

accuracy. Therefore, the scenarios and their weights have to be chosen carefully. The resulting values for \bar{E} can be found in table 4.1.

Table 4.1: Mean exactness coefficients for different algorithms and their standard derivation

Algorithm	\bar{E}
Synthetic data	1.000
BPD	0.746 ± 0.140
Abel inversion based algorithm with...	
-FVC	0.965 ± 0.118
-FHS	1.397 ± 0.230
-FLX-	0.861 ± 0.088
-FLX*	0.895 ± 0.063
-FLX+	0.935 ± 0.048
Tomography	0.899 ± 0.058

One can clearly see that the average result of the BPD algorithm is too low. Reasons for this will be discussed in sec. 4.3. The new Abel inversion based algorithm shows in general good, but a bit too low results, except when using the FHS camera for the divertor. The FHS values are too high, probably due to a double compensation. For the calculation of the FHS lines of sight only the Abel inversion was taken into consideration but not the compensation in the SOL. The FHS will be neglected in the further considerations.

Using the other cameras, the results are useful, but slightly too low. The standard deviation from the mean exactness is in the range from 5 to 10% . It is observed that the mean exactness with the FVC camera is higher than with the FLX, but instead the standard deviation of the latter is lower. As an alternative, one could take the mean values from the FVC and the FLX. The resulting mean exactness using FVC and FLX* would be $\bar{E} = 0.930 \pm 0.074$ which could serve as a compromise. Nevertheless, the new Abel inversion based algorithm shows significant improvement with respect to the BPD algorithm.

4.2 Evaluation of Several Synthetic Emissivity Profiles

The tomography is showing a quite small standard deviation but its mean exactness is around 10 percent too low. At this point it is important to remember that the tomography was performed using only the standard, non-optimized parameters. From fig. 4.9 it can be seen that an optimization of the tomography's parameters can increase its exactness significantly.

But also another effect can alter the exactness coefficient of the tomography and also of the other algorithms. As mentioned above, the selection of test-scenarios and their weights can have an influence on the results. Though it is not known how big this effect can be. Therefore, it can not be concluded why the coefficients in table 4.1 are too low for most of the algorithms. The reason can be statistical as well as an internal one of the algorithms. The latter assumption is indicated by the examination of the results for the most realistic emissivity profile in the previous chapter. An answer to the question of the error source might be provided by another evaluation with different scenarios.

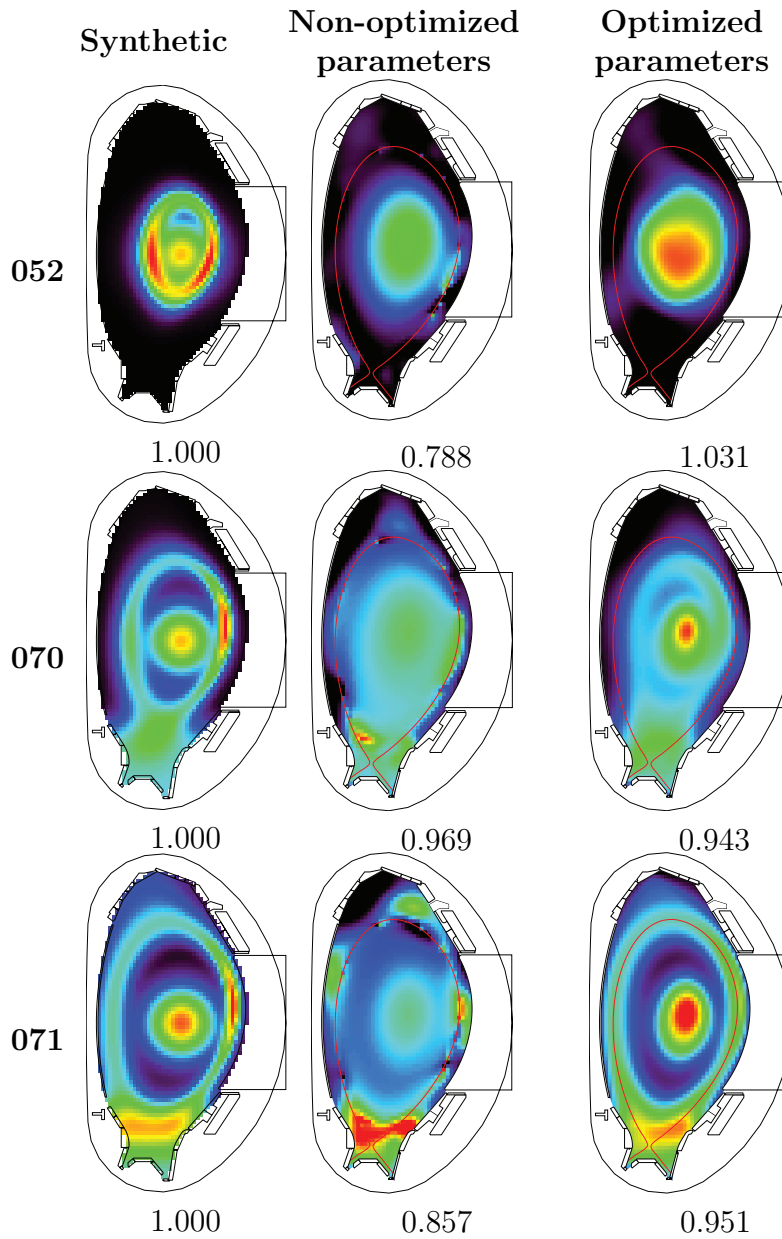


Fig. 4.9: The influence of optimized tomography parameters on its exactness. Scenarios from top to bottom: 052, 070, 071. On the left the synthetic emissivity profiles are depicted, in the middle the tomographic reconstructions with the standard (non-optimized) parameters, on the right the tomographic reconstructions with optimized parameters. The numbers below the profiles show the exactness of the corresponding reconstruction. Within one scenario, the colors are comparable (in horizontal direction). Optimizations performed by Matthias Bernert.

4.3 Error Mapping

To detect the sources of systematic inaccuracies, it is useful to look not only at one single scenario. The large quantity of different scenarios can be used to create a profile that shows in which regions an arbitrary algorithm is most susceptible for errors. Such a so-called error map can be received by overlapping the 93 scenarios that were introduced above. As the emissivity scale is different for each emissivity profile they were normalized. The overlapping was performed by calculating the mean value of the emissivity profiles, weighted by the weights that were defined in the previous section and by the deviations that the profiles had when applying the algorithm that is to examine. In fig. 4.10 the error maps for the non-optimized tomography, for the BPD algorithm, and for the above proposed mean value of FVC and FLX* can be seen.

An error map will only allow a statement about the probability of a deviation to happen if the radiation mainly comes from a certain plasma region. Though, it can give important insights into possible error sources of an algorithm.

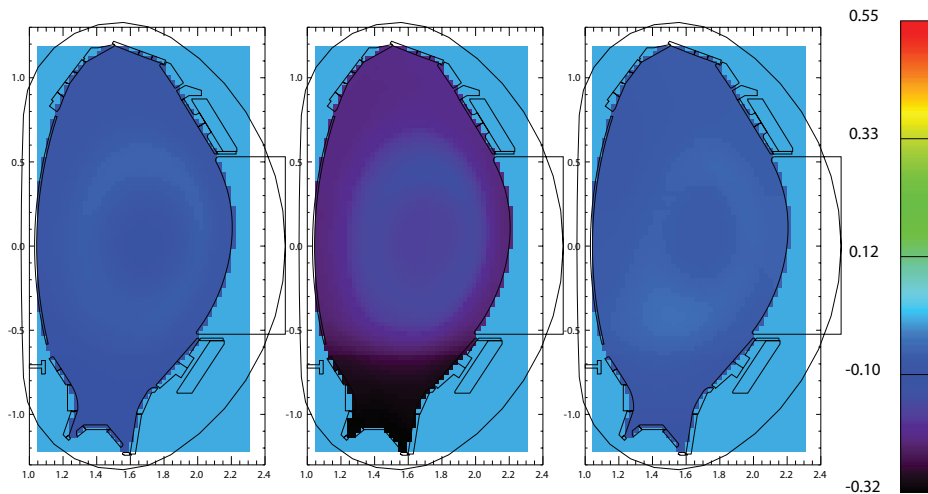


Fig. 4.10: Error maps of the different algorithms. From left to right: Tomography (with non-optimized parameters), BPD, Abel inversion based algorithm (mean value of FVC and FLX*). The colorbar is valid for all three error maps and indicates the mean deviation from the normalized nominal values.

4 Benchmarking and Application

In fig. 4.10 it can be observed that the BPD algorithm underestimates the divertor region by about 30 percent. This can explain the low accuracy of this algorithm. This effect is also confirmed by comparing single emissivity profiles.

It can also be observed that in the main chamber a circular structure with higher accuracy than the surrounding area occurs. This shows that BPD works best for poloidally symmetric radiation distributions in the main chamber which corresponds with the basic assumptions of this code. As a major part of the radiation normally comes from the divertor region, this behavior is disadvantageous for the operation of a plasma device. It might also explain why the BPD algorithm once worked and now doesn't.

The other algorithms don't show such irregularities. The error map of the tomography shows a very flat profile, in accordance with the low standard deviation of its mean exactness coefficient. Also the error map of the Abel inversion based algorithm (mean value of FVC and FLX*) does not show any regions with notable deviations from the nearly flat profile. For both algorithms, the tomography and the Abel inversion based algorithm, a faint circular structure is visible in the main chamber. It is not as strong as for the BPD algorithm, though. As many scenarios with ring-shaped radiation are in the used set of 93 scenarios, the weak rings in the error maps could be statistical artifacts. Despite this small deviation, no major issues are discernible in these error maps. In particular, there are no regions that seem to be preferred by the new Abel inversion based algorithm.

4.4 Application: Time Traces

Even though the previous section showed that the results of the new Abel inversion based algorithm are in good agreement with synthetic data and that this algorithm could be seen as an improvement in the calculation of $P_{rad,tot}$, it is important to examine its performance when calculating a time trace from actual plasma

discharges. For this, the Abel inversion based algorithm was applied on the bolometer data for 15 ms-averaged steps of a complete shot.

When examining a time trace there are a few indicators to detect if it is correct or not. One indicator is if the power balance matches. The total heating power P_{tot} should be equal to the power that is dissipated by the plasma, either by radiation ($P_{rad,tot}$) or by power directly deposited on the divertor plates and the other walls. While the power into the divertor (P_{div}) can be -more or less reliably- measured by infrared thermography (PLP diagnostic), there is no diagnostic that measures the power deposition on the first wall. Although this contribution is not in general negligible, we can assume it for ASDEX Upgrade to be very low compared to the other contributions (below 8% [33]).

4.4.1 Time Trace of Shot 31113

Fig. 4.11 shows a time trace for the ASDEX Upgrade shot 31113. The loss power calculated from the BPD algorithm plus P_{div} (from the thermography, PLP) is roughly the half of the heating power and, thus, clearly too low. The curves calculated with the Abel inversion based algorithm are higher.

The different time traces have a similar shape than the heating power which indicates the expected correlation of those two quantities under the given conditions. However, they don't match the power balance and are visibly lower. The differences could partially arise from the large measurement uncertainties of the thermography. As the neglected power deposition on the first wall is estimated to be lower than 8%, it can not serve as an explanation for the mismatch of the BPD algorithm, which is around 50%. However, considering the power that is deposited onto the first wall, the measurement uncertainties of the thermography and the possible 10% deviation of the Abel inversion based algorithm, the Abel inversion based algorithm's values are within the errorbars.

4 Benchmarking and Application

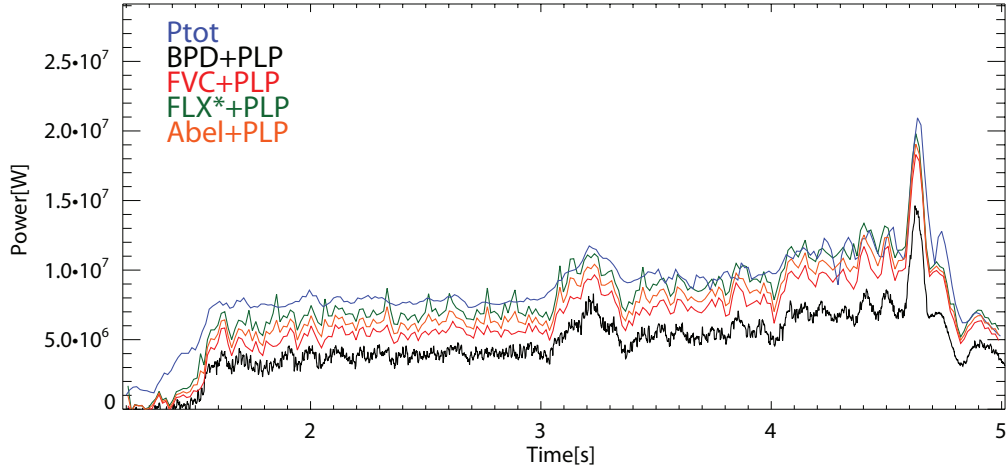


Fig. 4.11: Time trace of AUG shot 31113 with the total heating power (P_{tot} , blue line) and the reconstructed values of $P_{rad,tot}$ from the BPD algorithm (black line) and the Abel inversion based algorithm using the FVC (red line), the FLX* (green line) and the mean value of FVC and FLX* (orange line). On the reconstructed values the power onto the divertor plates was added (measured by the thermography, PLP).

4.4.2 Time Trace of Shot 31295

For shot 31295 the time traces are depicted in fig. 4.12. A power balance can not be examined as the thermography data is not available for this shot. Although one can not make any statement about the quantitative accuracy here, the curves still give useful qualitative information. It can be observed that the curves of the Abel inversion based algorithm have a similar profile shape than the P_{tot} curve and there are no indicators (like a change in the stored energy of the plasma W_{MHD}) for any deviation from that. The curve of the BPD algorithm, however, shows a completely other profile shape.

This difference can be explained by the location of the measured radiation. As it is apparent from fig. 4.13, where one bolometer line of sight faces the divertor and another the central region, the location of the dominant radiation changes over the time. In the beginning the divertor is dominating, followed by a phase with strong

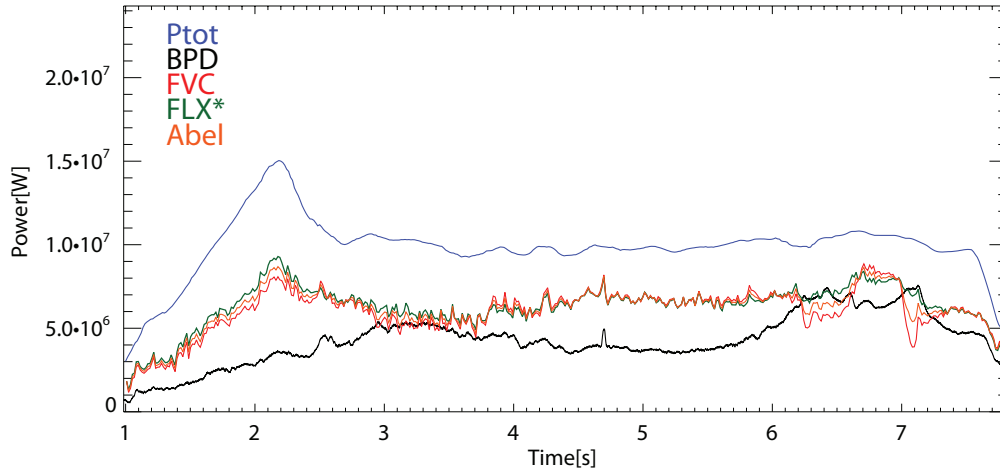


Fig. 4.12: Time trace of AUG shot 31295 with the total heating power (P_{tot} , blue line) and the reconstructed values of $P_{rad,tot}$ from the BPD algorithm (black line) and the Abel inversion based algorithm using the FVC (red line), the FLX* (green line) and the mean value of FVC and FLX* (orange line).

central impurity radiation between 2.5 s and 4.5 s, another divertor radiation phase from 4.5 s to 5.5 s and from there on again high central radiation.

It can be observed that in phases with dominating main chamber radiation, the two algorithms are in good agreement. With dominating divertor radiation, the BPD declines while the Abel inversion based algorithm's curve still resembles the shape of the P_{tot} curve. With the knowledge out of sec. 4.3, we know that the BPD algorithm reproduces this wrong and the Abel inversion based algorithm appears to be more accurate. The Abel inversion based algorithm instead seems to give reasonable results also for scenarios with high divertor radiation.

4.4.3 Time Trace of Shot 30503

Another example for the different recognition of divertor radiation of the two algorithms can be observed in shot 30503. As fig. 4.14 shows, the BPD curve slowly

4 Benchmarking and Application

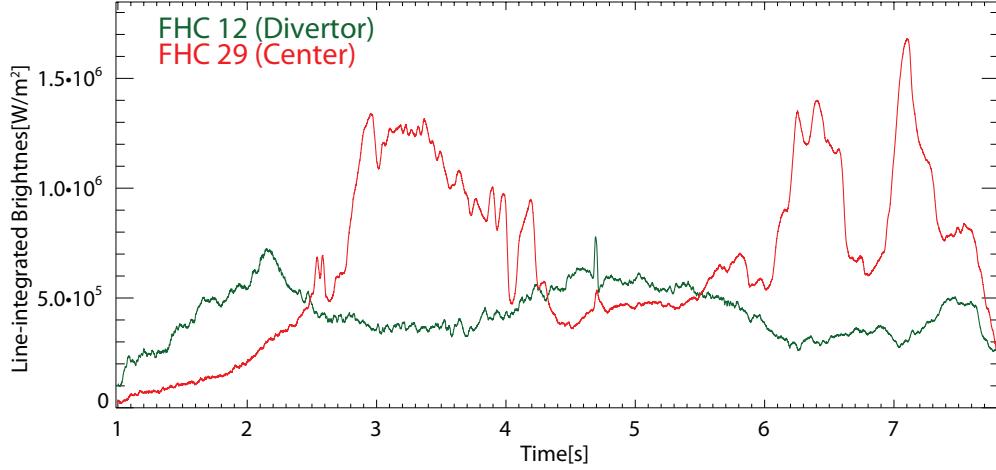


Fig. 4.13: Measurements of FHC lines of sight 12 (facing the divertor) and 29 (facing the center). One can observe that twice impurities accumulate in the core between 2.5 s and 4.5 s and from 5.5 s on.

increases (particularly from 4.5 s on) while the Abel inversion based algorithm remains constant, following the shape of the P_{tot} curve. The BPD's and the Abel inversion based algorithm's values are too low since the thermography signals are not utilizable. As the P_{div} is missing, it can in principle not be decided which algorithm gives the right value. However, as it was the aim of this shot to have a high radiative power fraction, the curves of the Abel inversion based algorithm with a power fraction of around 75% of the heating power are more credible than that of the BPD with only 35% (2.5 – 4.5 s) to 55% (peak at 5.5 s).

The reason for the differences can be found in the origin of the radiation. As fig. 4.15 shows, gases were puffed into the plasma, changing its radiation. In this shot nitrogen and krypton were injected, using a feedback control so that the radiated power is supposed to remain constant up to the third krypton level. In the beginning, purely nitrogen was puffed in the plasma, being stepwise replaced by krypton over the time.

It can be observed that with the increasing krypton concentration and the decreasing nitrogen concentration the BPD curve rises (while the Abel inversion

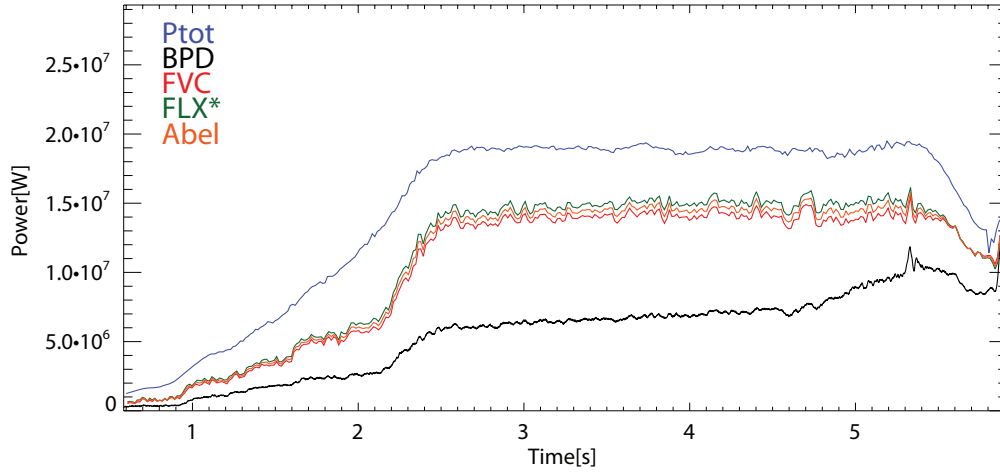


Fig. 4.14: Time trace of AUG shot 30503 with the total heating power (P_{tot} , blue line) and the reconstructed values of $P_{rad,tot}$ from the BPD algorithm (black line) and the Abel inversion based algorithm using the FVC (red line), the FLX* (green line) and the mean value of FVC and FLX* (orange line).

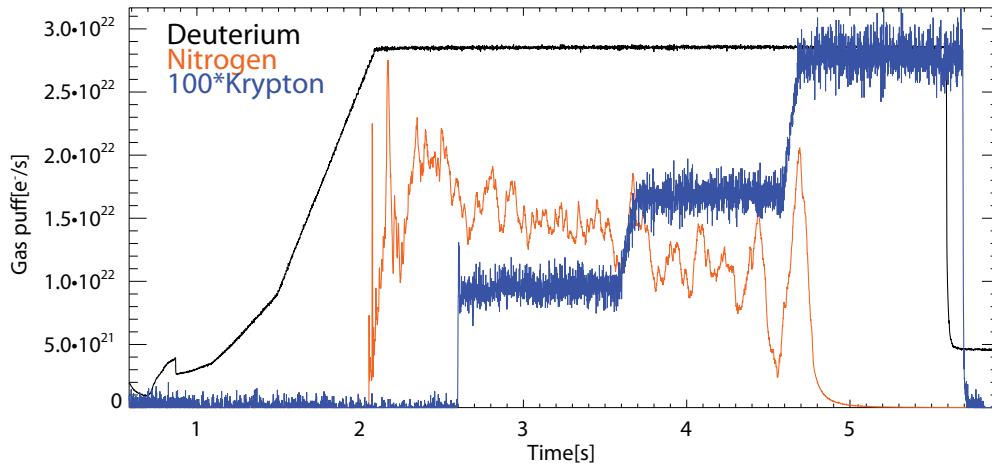


Fig. 4.15: Number of particles puffed in the plasma. The nitrogen puff (orange line) is reduced as the krypton puff (blue line) is increased. The nitrogen puff is feedback-controlled so that the total amount of radiation remains constant. Nitrogen preferably radiates in the divertor, krypton in the edge.

4 Benchmarking and Application

based algorithm remains constant). As shown in chapter 2.1.4 nitrogen radiates dominantly in the divertor region whereas krypton forms a radiating ring in the edge. With increasing abundance of krypton the location of the major part of the radiation changes from the divertor to the main chamber. The behavior of the BPD or Abel inversion based algorithm, respectively, is again in line with the previous observations. The BPD algorithm underestimates the divertor and is optimized for circular symmetric radiation from the main chamber. The new Abel inversion based algorithm instead does not show this behavior while giving reasonable results.

5 Summary and Conclusion

After many years in operation, the BPD algorithm recently turned out to be not accurate enough for present conditions. In this thesis a new $P_{rad,tot}$ algorithm, based on an Abel inversion, was implemented and tested. For the latter, a program for the creation of synthetic radiation profiles was written.

The new algorithm uses an Abel inversion in order to calculate the radiation coming from the main chamber plasma. The basic assumption of an Abel inversion is that the plasma forms zones along the magnetic flux surfaces that have a constant emissivity. Such zones of constant emissivity are each defined by one line of sight. In the new algorithm, the lines of sight of the FHC camera that lay above the magnetic axis were chosen in order to perform an Abel inversion. When comparing the lines of sight in the lower main chamber (that are not facing into the divertor), it was observed that the measurements of those lines are not according to the calculation of the Abel inversion. The measured line-integrated brightness increases towards the divertor. The new algorithm assumes that the excess radiation is coming from the high field side SOL. The excess power is placed into small areas that cover the SOL. To get an estimate of the radiation that is coming from the divertor, three cameras, which are observing the divertor, can be used. The contribution of the area that is already covered by the Abel inversion is subtracted and the excess power distributed equally over the area that is covered by the respective lines of sight. For the divertor legs, the measured power of the corresponding bolometer cameras was distributed equally over the area they cover. As the FLX camera is (unlike the FVC and the FHS) vertically orientated, three scenarios for the location of the divertor radiation along the lines of sight were considered: radiation

5 Summary and Conclusion

at the most inner point (FLX-) at the most outer point (FLX+) or in the areas barycenter (FLX*). $P_{rad,tot}$ can be determined by summing up the contributions of each subarea.

To benchmark the new algorithm, synthetic emissivity profiles were used. A program introduced in this thesis was used to create a set of synthetic poloidal emissivity profiles and to calculate out of this the synthetic measurements of the bolometry. Those data were given to the BPD algorithm, to the Abel inversion based algorithm and to the tomography in order to calculate a value for $P_{rad,tot}$ which was then compared to the value from the synthetic profile. An evaluation of single profiles shows deviations of around 10% for the Abel inversion based algorithm (using FVC or FLX) for realistic profiles. If, in contradiction to the code's assumption, the profile is not completely poloidally symmetric, it can result in uncertainties of around 15%. For certain radiation distributions (as such with poloidal asymmetries on the HFS), the corrections in the high field side SOL and the approach for the divertor can not compensate the errors of the Abel inversion as intended, resulting in an underestimation of $P_{rad,tot}$. These scenarios have a low probability to occur in a tokamak plasma, though. The BPD algorithm works best for central circular symmetric radiation profiles, for which it was optimized. However, divertor radiation is underestimated, which could be the reason for the recent inaccuracy of the BPD. In general, the tomography (using non-optimized parameters) gives results with a deviation margin below 10%. For a more reliable statement about the algorithms' accuracy, a statistical evaluation is necessary. As not all profiles in the set are equally likely to occur in a tokamak, they were assigned statistic weights. The evaluation of the whole set leads to the conclusion that the results of the BPD algorithm are on average 25% too low. This results from the underestimation of the divertor. The Abel inversion based algorithm is on average only 5% (using FVC) to 15% (FLX-) too low. This deviation could be reduced to 7% by calculating the mean value of FVC and FLX*, as this could compensate errors that are only occurring for one camera. In general, the results of the Abel inversion based algorithm are within the deviation margins of 10%. This could result from violations of the algorithms basic assumption of poloidal symmetry.

The tomography is about 10% too low, but optimizing its input parameters can increase the exactness.

As a method to find sources of systematic inaccuracies of an algorithm for specific regions of the poloidal plasma cross-section, error maps were introduced. As a weighted mean-value of all emissivity profiles these can indicate the regions that are eventually over- or underestimated by an algorithm. For the tomography and for the Abel inversion based algorithm they show a flat profile and no specific regions causing deviations. This indicates that also the 10% deviation of the Abel inversion based algorithm is distributed equally. In the map of the BPD algorithm instead, it was observed that the divertor radiation is underestimated by around 30% and only the radiation from the confined plasma is detected correctly. As further shown in this work, a changing radiation in the divertor during a plasma discharge can lead to false conclusions.

To validate the new Abel inversion based algorithm in application, some time traces of complete shots of ASDEX Upgrade were calculated. One indicator to test a $P_{rad,tot}$ algorithm is the match of the power balance. The total heating power (P_{heat}) is dissipated by radiation ($P_{rad,tot}$) and deposited on the divertor plates (P_{div} , determined by infrared thermography) and a minor part over the first wall (not measured). For two shots it could be shown that the Abel inversion based algorithm's results are more credible than those of the BPD algorithm as the BPD algorithm was reacting on changes of the radiation distribution, e.g. by core accumulations or impurity seeding, while the Abel inversion based algorithm remains stable.

Several reasons can cause that the BPD algorithm now does not work accurate for the current plasma conditions although it was benchmarked and tested when it was introduced. Over the years, ASDEX Upgrade underwent many changes that affected the radiation behavior of the plasma. The divertor design was changed several times and from 1999 to 2007 the material of the plasma facing components was gradually changed from carbon to tungsten. Also changes in the camera design and configuration could have an influence on the BPD algorithm's accuracy. Since

5 Summary and Conclusion

the BPD algorithm was introduced, the cameras were renewed and lately also the interior of the FVC camera (that the BPD is relying on) was changed in order to minimize internal reflections. In general, the evaluations showed that the BPD algorithm nowadays has serious issues and it should not be used unquestioned. The Abel inversion based algorithm instead can give results within an deviation margin of 10% with an error of about 10% for realistic scenarios.

5.1 Outlook

Even though the results of the Abel inversion based algorithm are satisfactory, further improvements are possible and necessary. As seen in sec. 4.2.1, the code's result when using FVC for the divertor differs from the result with FLX*. In sec. 4.2.2 a possible solution was shown by combining the two methods in order to increase the exactness. Also the combination of other cameras are possible. Further testing will be necessary in order to find the best way to treat the inaccuracy of single cameras in certain scenarios.

For its potential future usage it is important that the code can calculate the time trace of a shot (max. 10s) in a reasonable amount of time, typically within a few minutes after the shot. The run time of the code has to be tested and improved in order to meet this condition. Another possible improvement could be to take a fixed magnetic flux profile. In case this turns out to be useful, the code could be converted into a linear matrix equation with fixed coefficients (see eq. (3.9)), creating the possibility of a real time analysis of $P_{rad,tot}$.

Before doing this, the deviation of around 10% in the statistical evaluation for the Abel inversion based algorithm and for the tomography should be examined. It is not completely clear yet, if this deviation is an intrinsic deviation of the examined algorithms or caused by the evaluation method. The comparison with other, yet to implement, algorithms can be considered. On the basis of this thesis, the necessary tools are now available.

A Bibliography

- [1] J. Wesson. *Tokamaks*. Oxford University Press, 2004.
- [2] Max-Planck-Institut für Plasmaphysik. *IPP Bilddatenbank. Grafik: Dr. Christian Brandt*. 2011.
- [3] Max-Planck-Institut für Plasmaphysik. *Homepage of the IPP (including subpages)*. 2015. URL: <http://www.ipp.mpg.de>.
- [4] M. Bernert. “Analysis of the H-mode density limit in the ASDEX Upgrade tokamak using bolometry”. PhD thesis. Fakultät für Physik der Ludwig-Maximilians-Universität München, durchgeführt am Max-Planck-Institut für Plasmaphysik, Garching bei München, 2013.
- [5] H. Meister et al. “Broad-band efficiency calibration of ITER bolometer prototypes using Pt absorbers on SiN membranes”. In: *Review of Scientific Instruments* 84.12 (2013), p. 123501.
- [6] R. Neu. “High- Z plasma facing components in fusion devices: boundary conditions and operational experiences”. In: *Physica Scripta* 2006.T123 (2006), p. 33.
- [7] J. C. Fuchs et al. “Radiation Distribution in the Full Tungsten ASDEX Upgrade”. In: *35th EPS Conference on Plasma Physics in Hersonissos, Greece*. Vol. 32D. ECA. European Physical Society, 2008, P.–2.012.
- [8] J. Fuchs et al. “Detailed Investigation of the Divertor Radiation in ASDEX Upgrade”. In: *29th EPS Conference on Plasma Physics in Montreux, Switzerland*. Vol. 26B. ECA. European Physical Society, 2002, P.–1.047.

A Bibliography

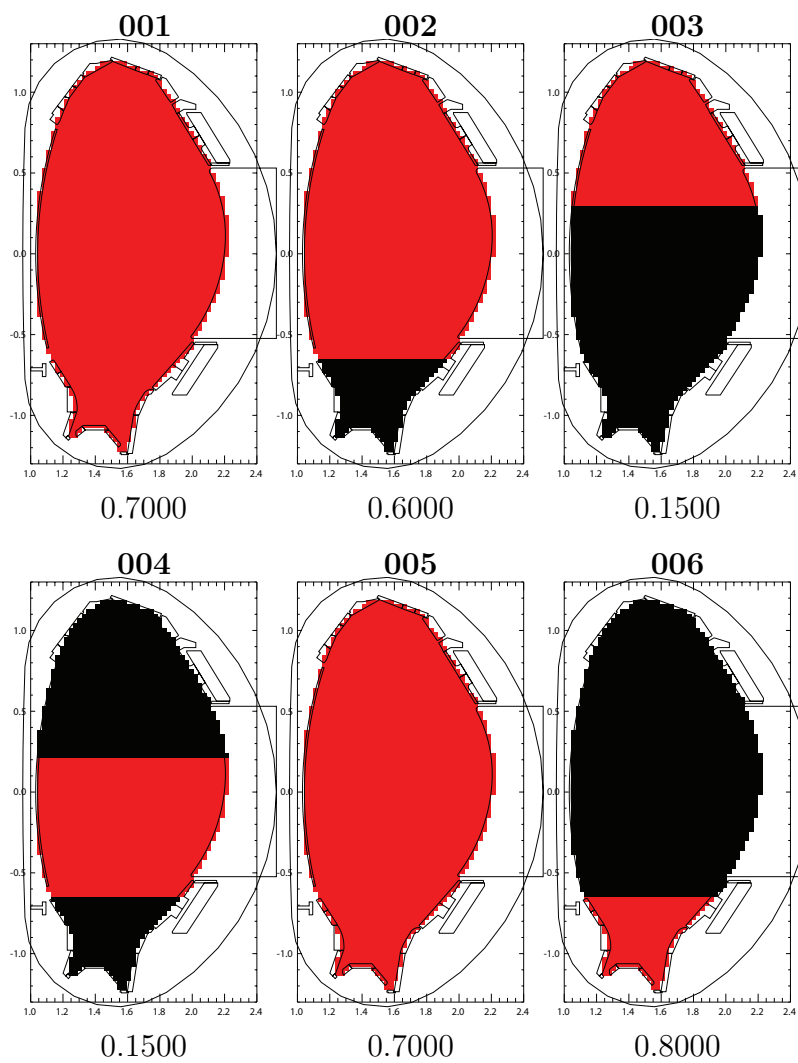
- [9] J. C. Fuchs et al. “Radiation Distribution During Impurity Seeding Experiments in the Full Tungsten ASDEX Upgrade”. In: *36th EPS Conference on Plasma Physics in Sofia, Bulgaria*. Vol. 33E. ECA. European Physical Society, 2009, P–1.147.
- [10] J. Fuchs et al. “Radiation distribution and power balance in the ASDEX Upgrade LYRA divertor”. In: *Journal of Nuclear Materials* 290-293 (Mar. 2001), pp. 525–529.
- [11] M. Tokar. “Impurity Transport and Radiation”. In: *Transactions of Fusion Science and Technology* 61 (2012), pp. 213–220.
- [12] T. Pütterich et al. “Impurity Limits in a Reactor Grade Fusion Device”. In: *42nd EPS Conference on Plasma Physics in Lisbon, Portugal*. 2015, P4.111.
- [13] T. Pütterich. *Private communication*. October 2015.
- [14] A. Kallenbach et al. “Impurity seeding for tokamak power exhaust: from present devices via ITER to DEMO”. In: *Plasma Physics and Controlled Fusion* 55.12 (Nov. 2013), p. 124041.
- [15] G. Matthews. “Plasma detachment from divertor targets and limiters”. In: *Journal of Nuclear Materials* 220–222 (1995). Plasma-Surface Interactions in Controlled Fusion Devices, pp. 104–116.
- [16] U. Wenzel et al. “Spatial radiation profiles in the ASDEX upgrade divertor for detached plasmas”. In: *Journal of Nuclear Materials* 241-243 (1997), pp. 728–733.
- [17] M. Bernert et al. “High radiation scenarios with radiation inside the confined region at ASDEX Upgrade”. In: *42nd EPS Conference on Plasma Physics in Lisbon, Portugal*. 2015, P1.135.
- [18] International Radiation Detectors, Inc. 2527 West 237th Street Unit A, Torrance, CA 90505-5243. <http://www.ird-inc.com>.
- [19] M. Bernert. “Bolometry with diodes at the tokamak ASDEX Upgrade”. Diploma Thesis. Physics Department of the Technische Universität München, performed at the Max-Planck-Institut für Plasmaphysik (IPP), Garching, 2010.

- [20] I. Hutchinson. *Principles of Plasma Diagnostics*. Cambridge University Press, 2005.
- [21] W. Schneider et al. “ASDEX Upgrade MHD equilibria reconstruction on distributed workstations”. In: *Fusion Engineering and Design* 48 (Aug. 2000), pp. 127–134.
- [22] L. Ingesson. “Chapter 7 Tomography Diagnostics: Bolometry and Soft-X-Ray Detection”. In: *Fusion Science and Technology* 53 (2008), pp. 528–576.
- [23] G. Herman. *Image Reconstruction From Projections. The Fundamentals of Computerized Tomography*. Academic Press, 1980.
- [24] F. Natterer and F. Wübbeling. *Mathematical Methods in Image Reconstruction*. Society for Industrial and Applied Mathematics, 2001.
- [25] T. Peters. *CT Image Reconstruction*. 44th AAPM Annual Meeting, Montreal. 2002. URL: <https://www.aapm.org/meetings/02AM/pdf/8372-23331.pdf>.
- [26] M. Schneider. “Regularisierung der Bolometer-Tomografie an ASDEX Upgrade mittels realistischer Diffusionskoeffizienten”. MA thesis. Max-Planck-Institut für Plasmaphysik and LMU München, 2011.
- [27] J. C. Fuchs et al. “Twodimensional Reconstruction of the Radiation Power Density in ASDEX Upgrade”. In: *21st EPS Conference on Controlled Fusion and Plasma Physics*. Vol. 18B, Part 3. ECA. European Physical Society, 1994, pp. 1308–1311.
- [28] C. Fuchs. *Private communication*. October 2015.
- [29] M. Bernert et al. *Recent Improvements of Bolometry at ASDEX Upgrade*. Edge Physics Seminar. IPP Garching, Dec. 17, 2012.
- [30] N. Joshi, P. Atrey, and S. Pathak. “Abel inversion of asymmetric plasma density profile at Aditya tokamak”. In: *Journal of Physics: Conference Series* 208 (Feb. 2010), p. 012129.
- [31] S. Potzel et al. “A new experimental classification of divertor detachment in ASDEX Upgrade”. In: *Nuclear Fusion* 54.1 (2014), p. 013001.
- [32] M. Bernert. *Private communication*. October 2015.

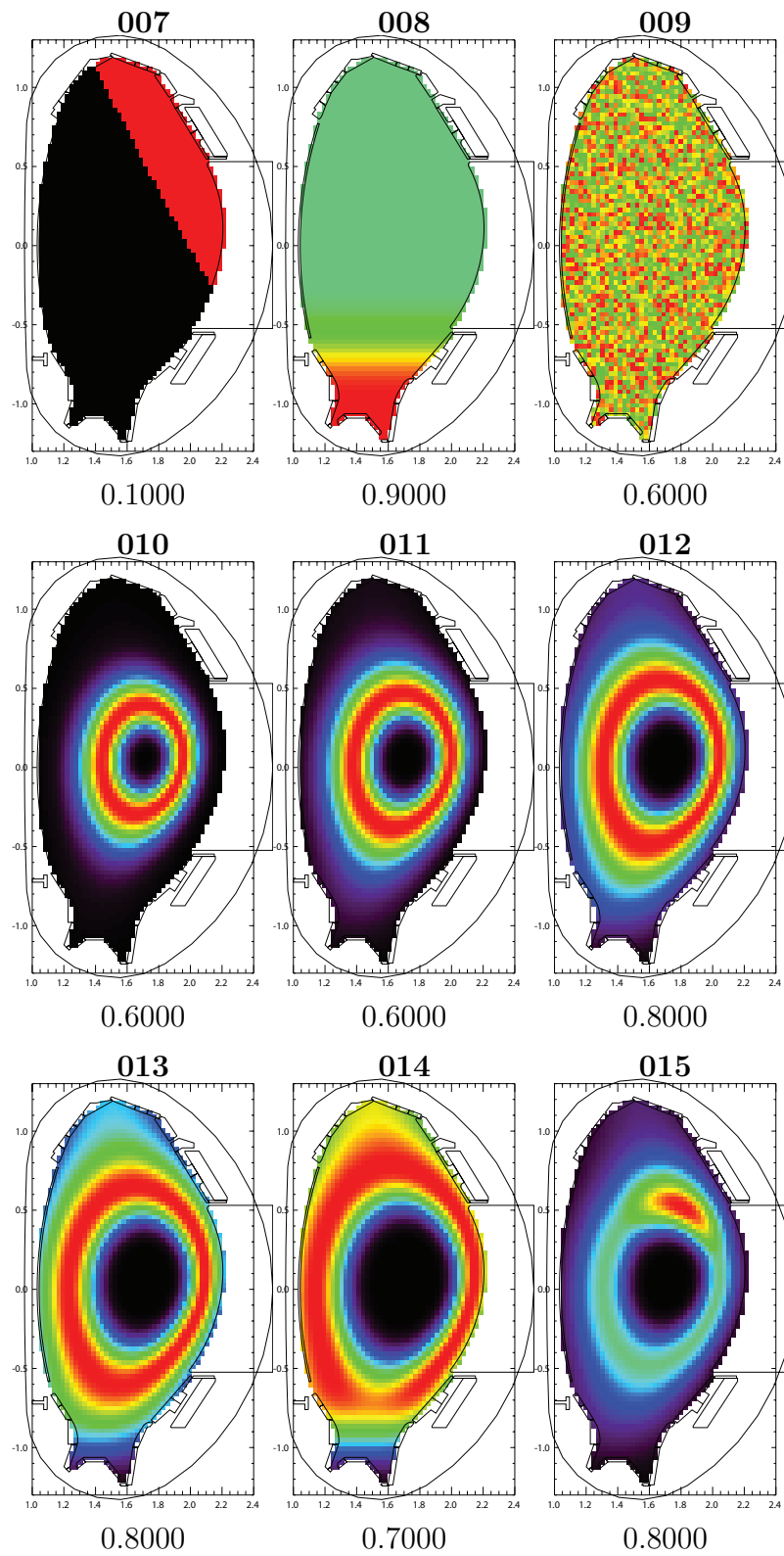
A Bibliography

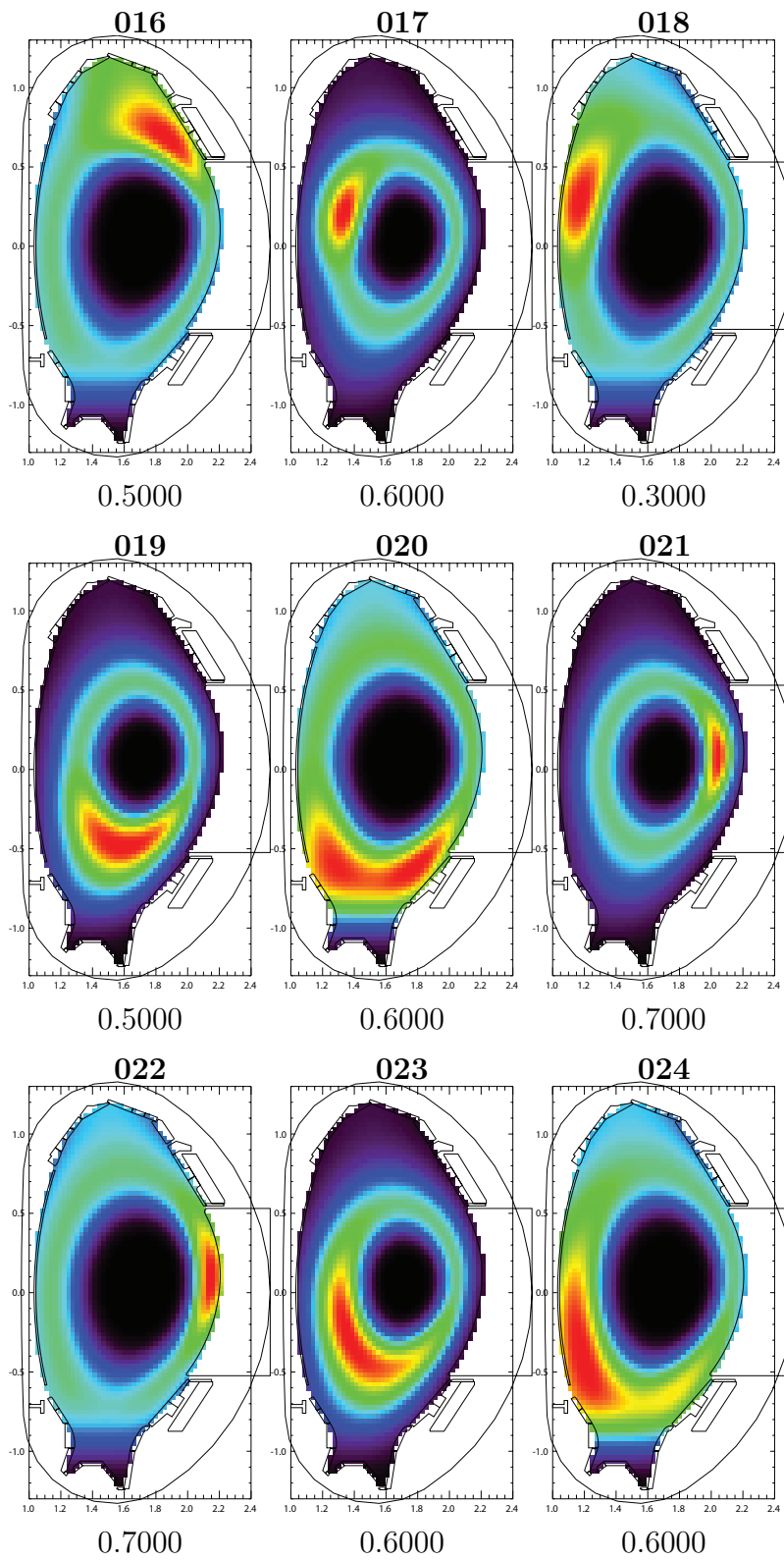
- [33] A. Herrmann et al. “Power deposition outside the divertor in ASDEX Upgrade”. In: *Plasma Physics and Controlled Fusion* 46.6 (2004), p. 971.
- [34] J. Fuchs et al. “Variation of radiation profiles with plasma parameters in ASDEX Upgrade”. In: *26th EPS Conference on Plasma Physics in Maastricht, The Netherlands*. Vol. 23J. ECA. European Physical Society, 1999, pp. 1385–1388.
- [35] L. Ingesson. *The Mathematics of some Tomography Algorithms used at JET*. JET-R(99)08. JET Joint Undertaking, 2000.
- [36] F. Natterer. *The Mathematics of Computerized Tomography*. Wiley, 1986.

B Synthetic Emissivity Profiles

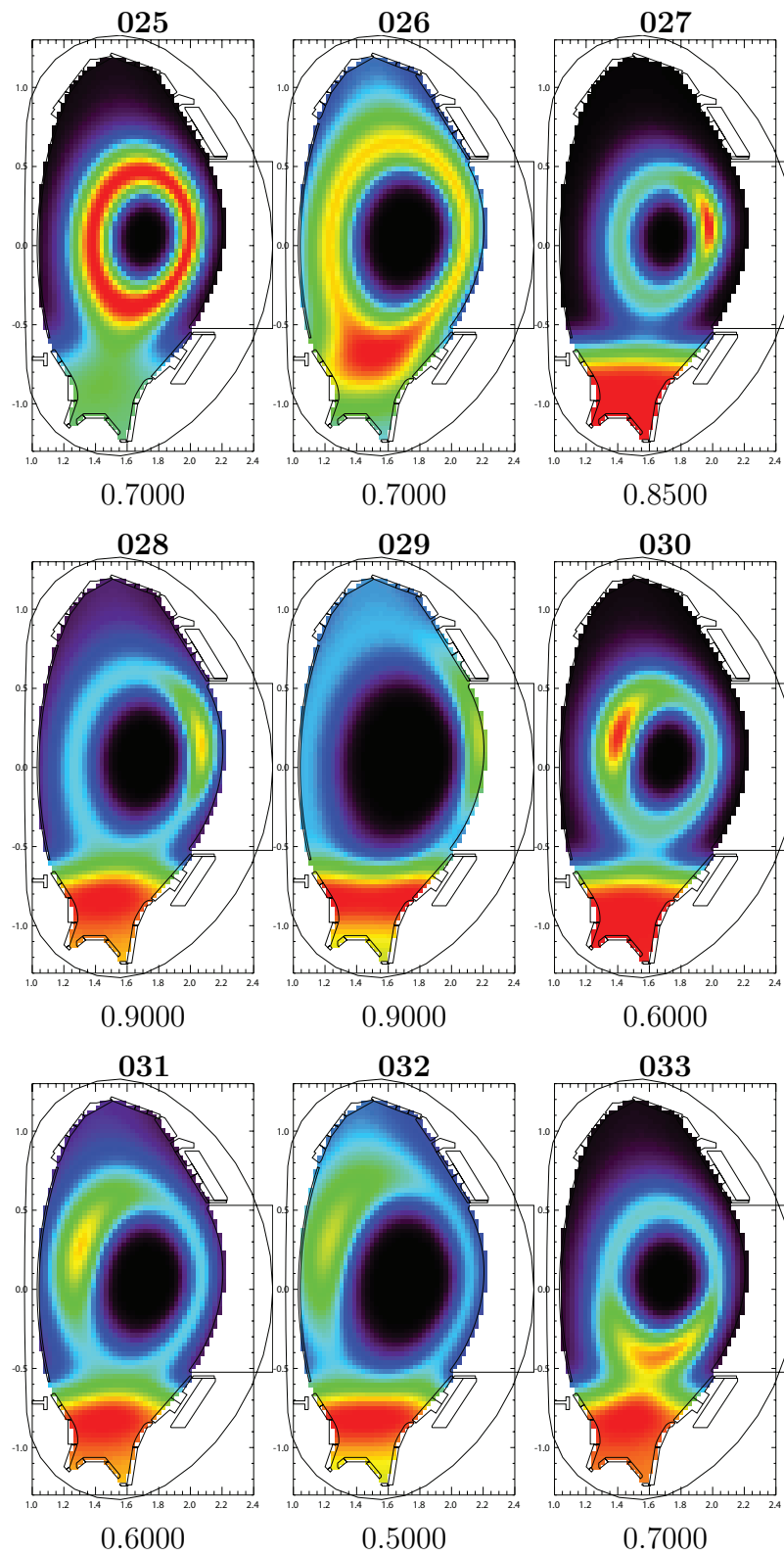


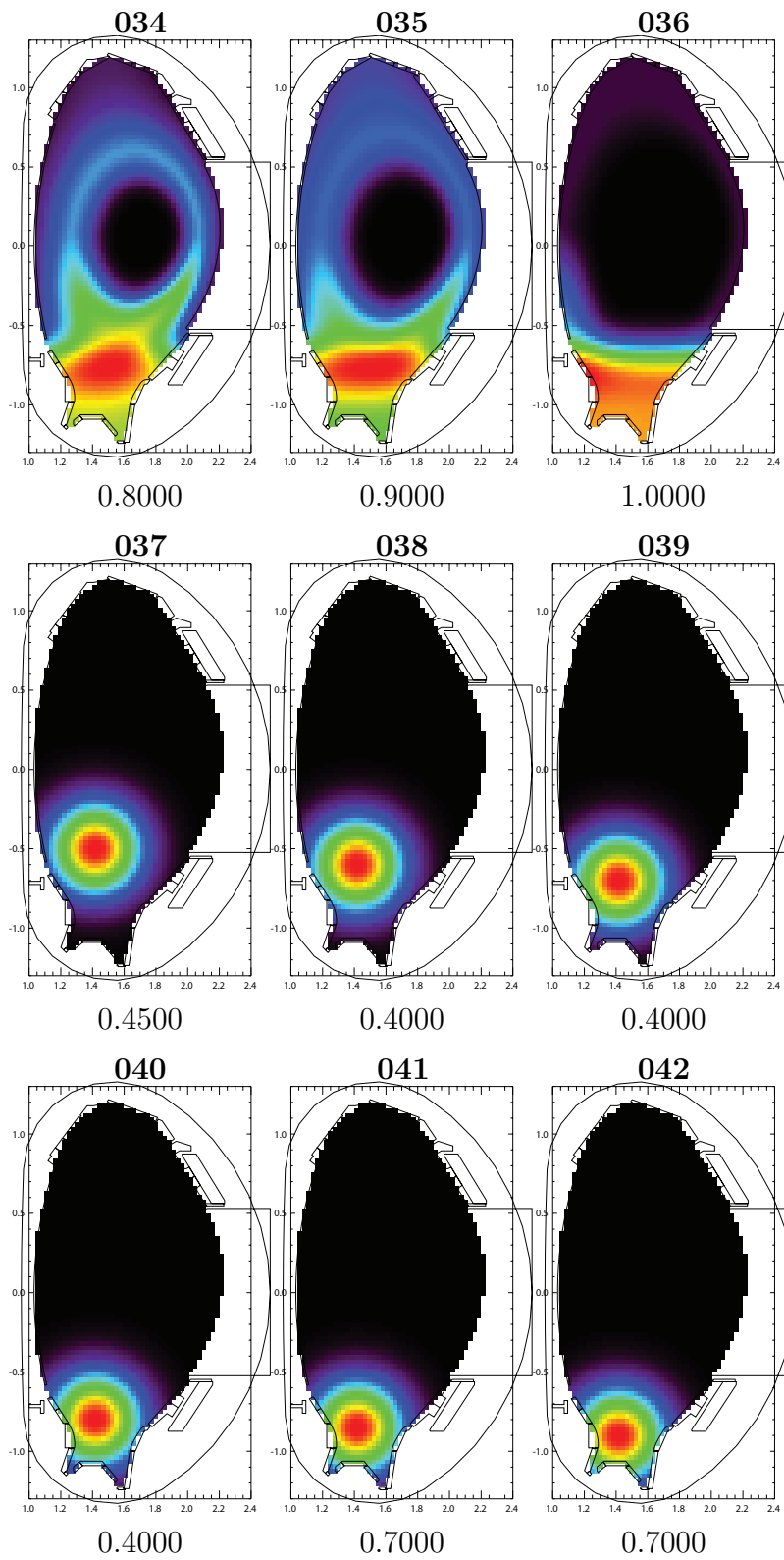
B Synthetic Emissivity Profiles



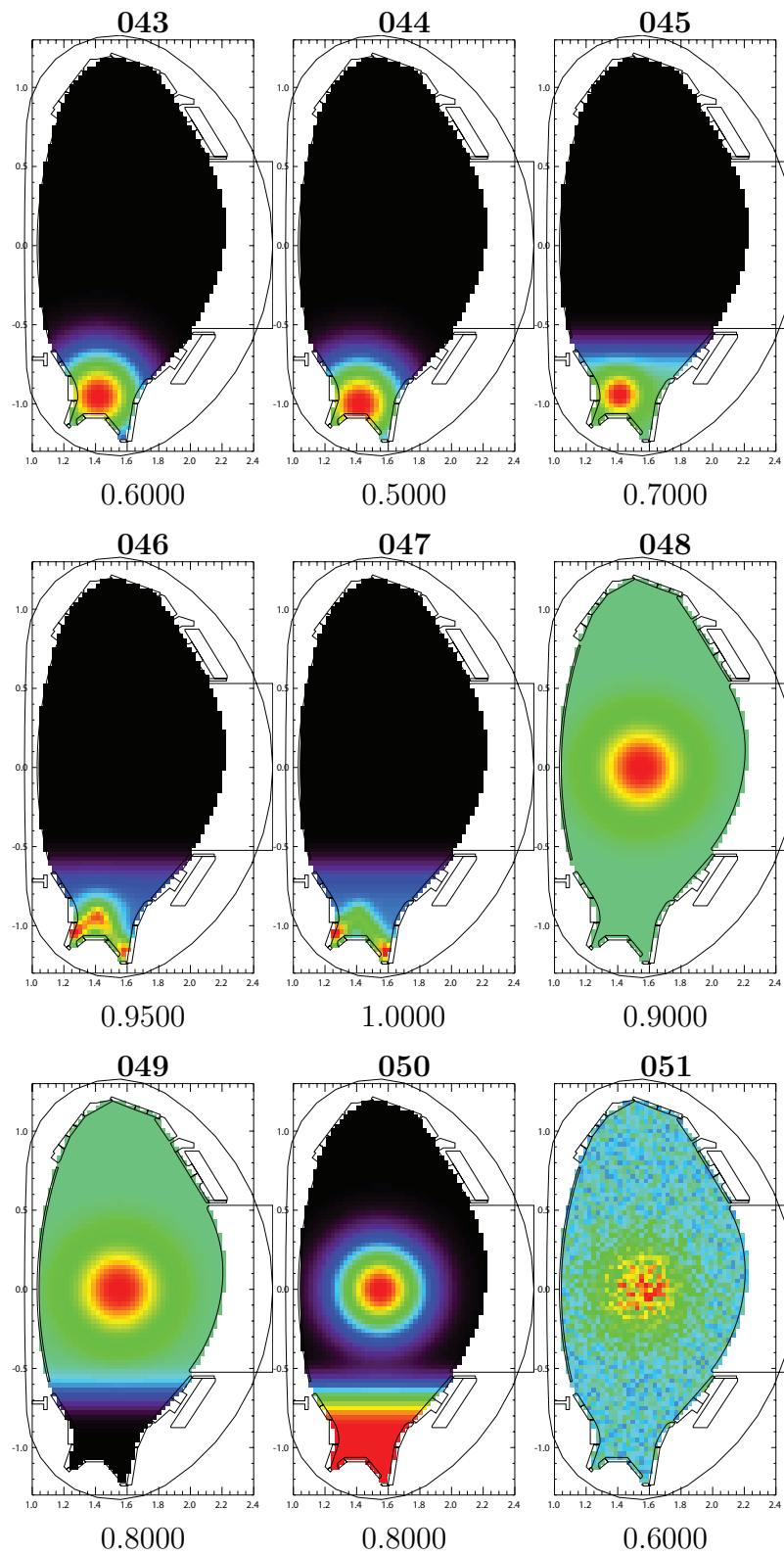


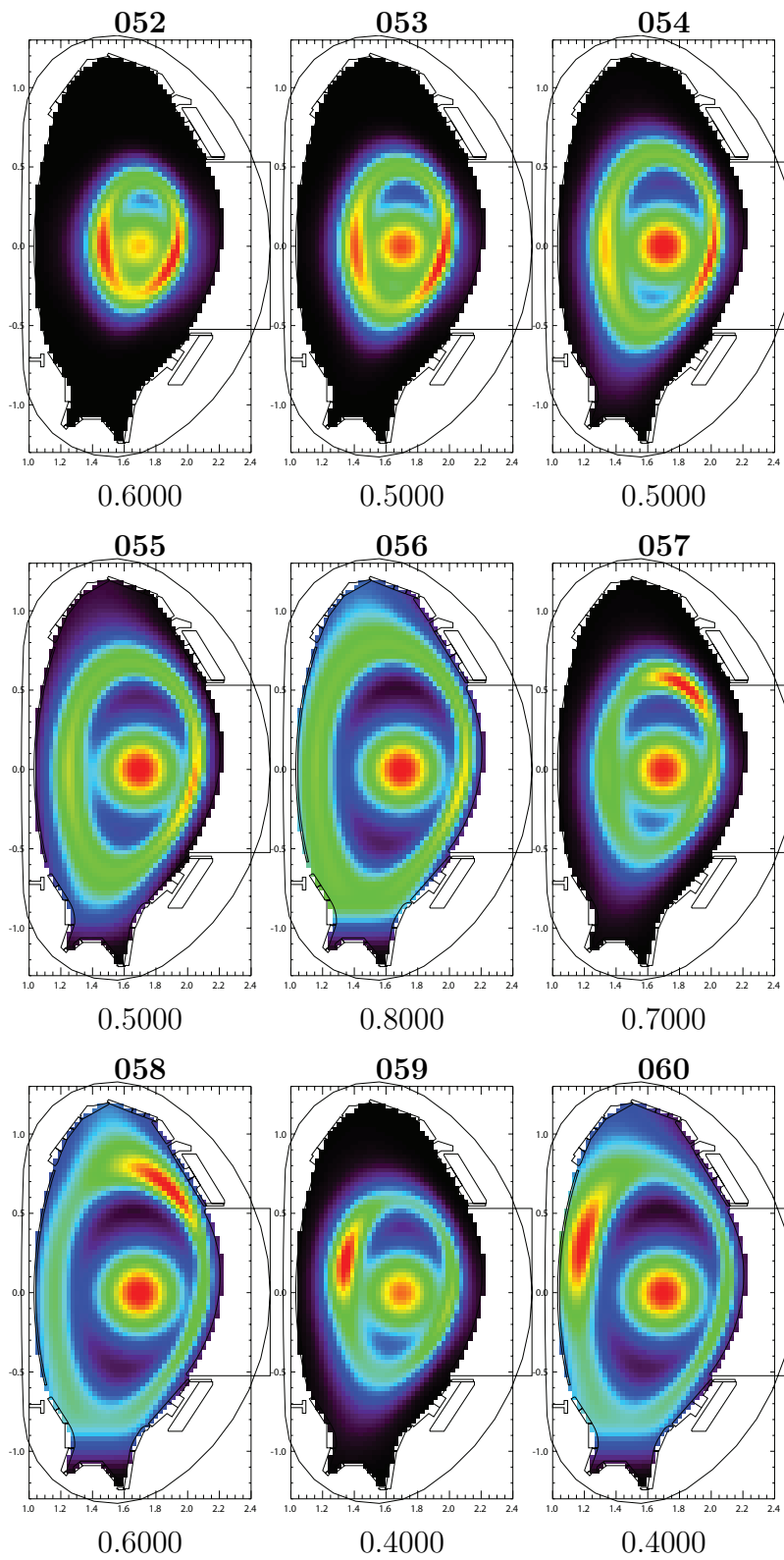
B Synthetic Emissivity Profiles



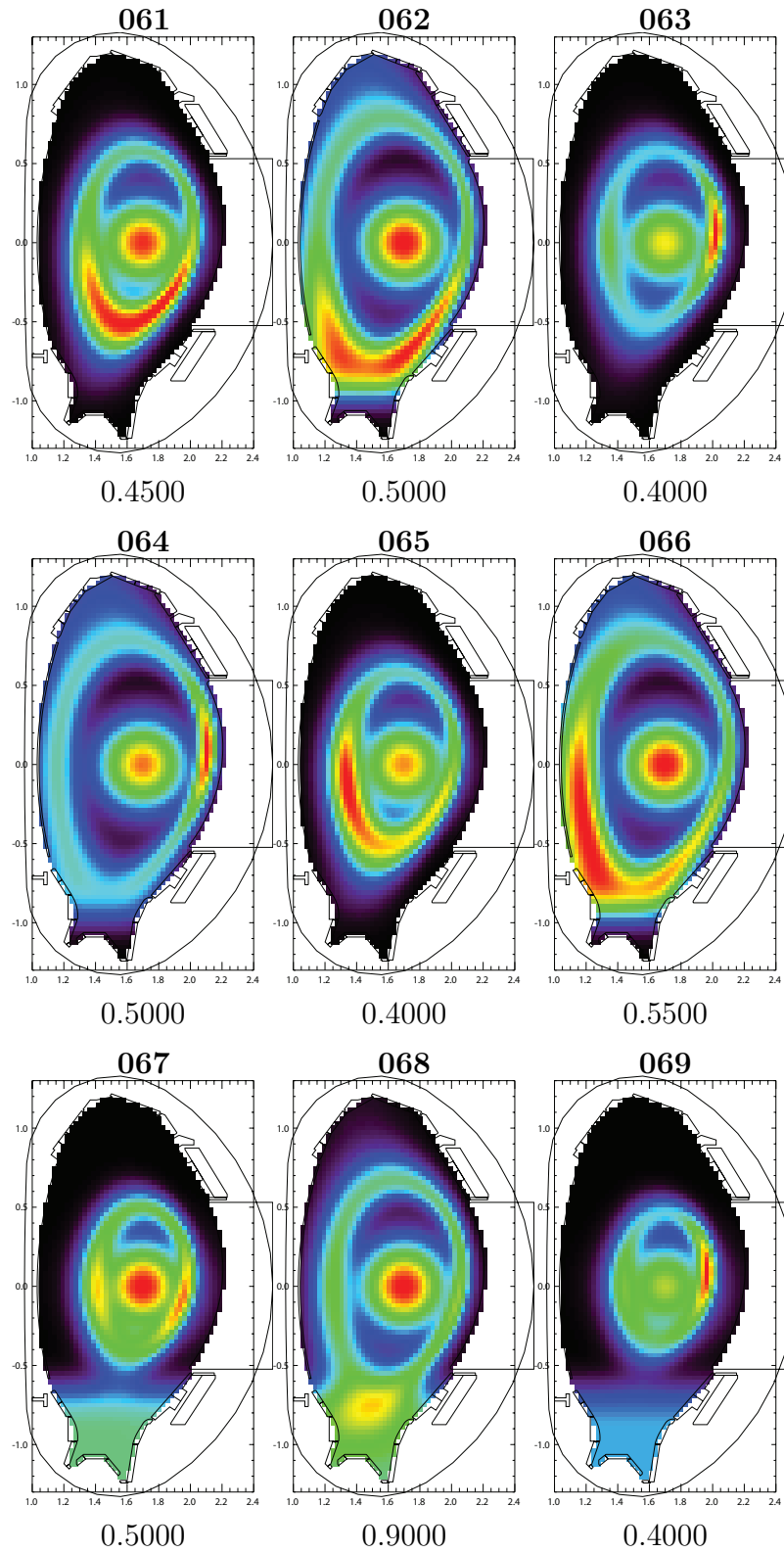


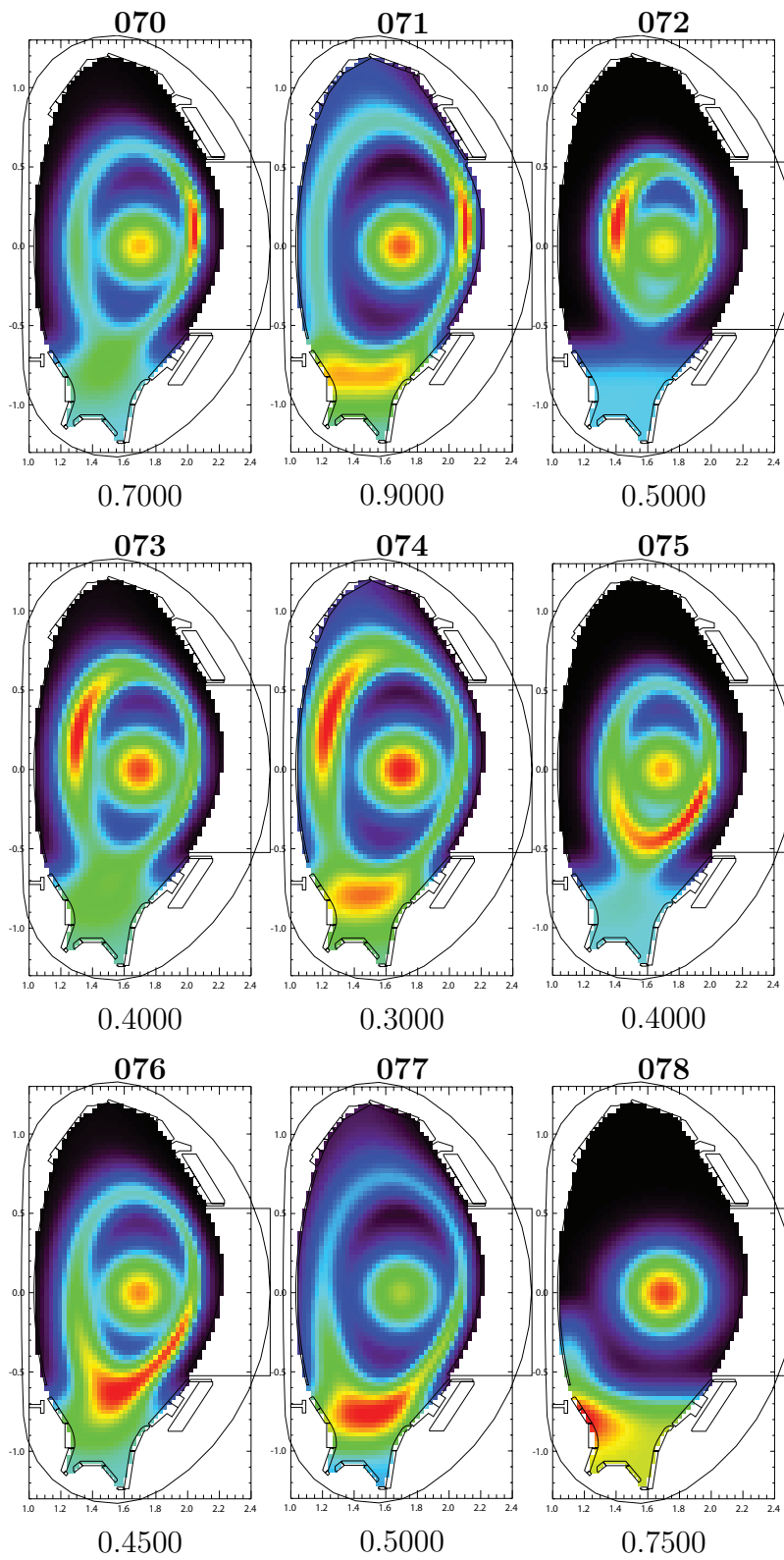
B Synthetic Emissivity Profiles



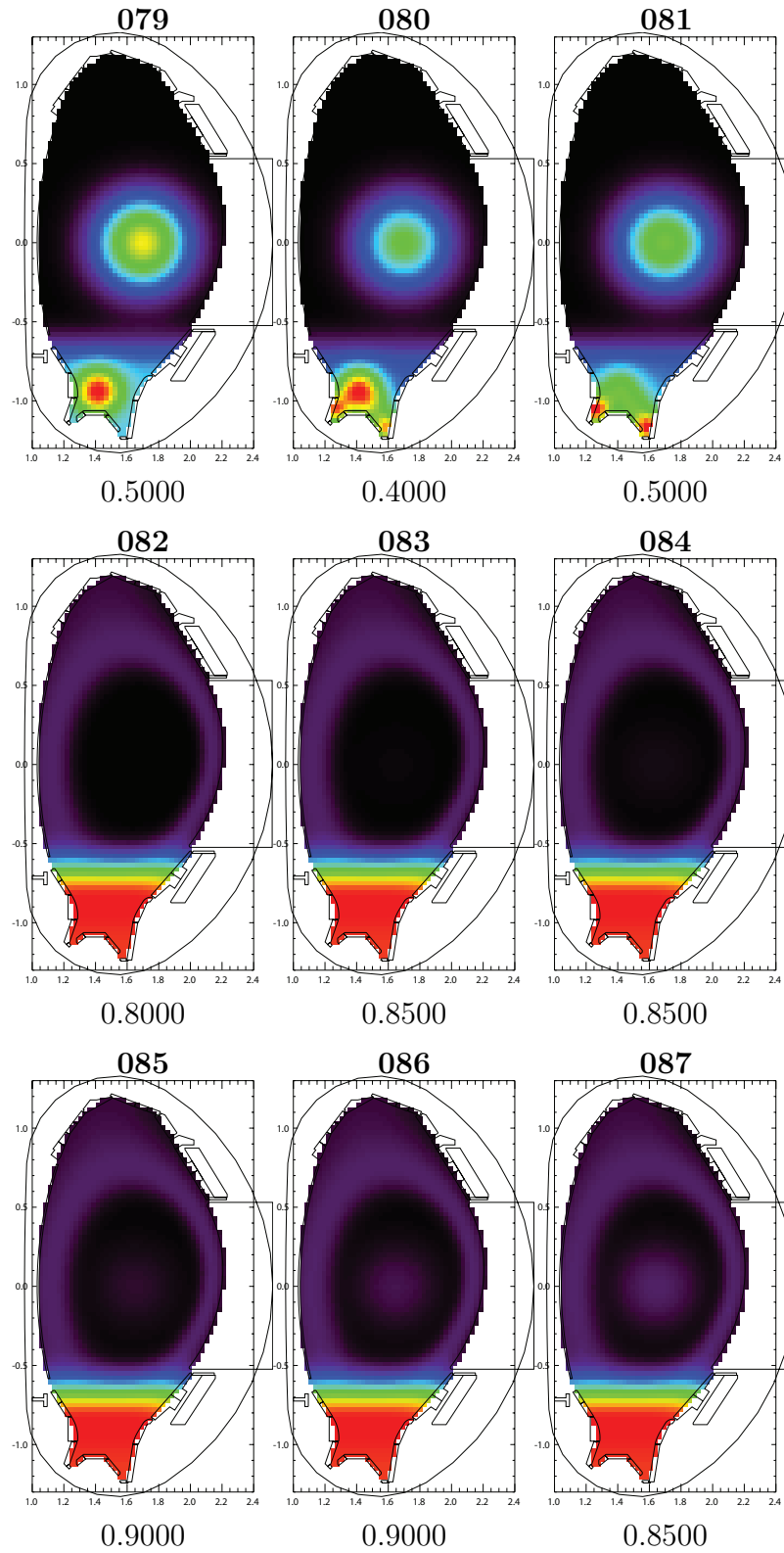


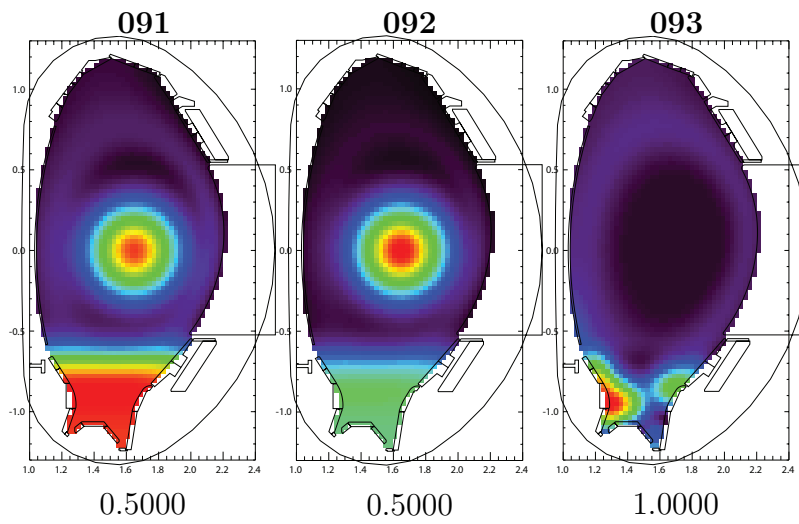
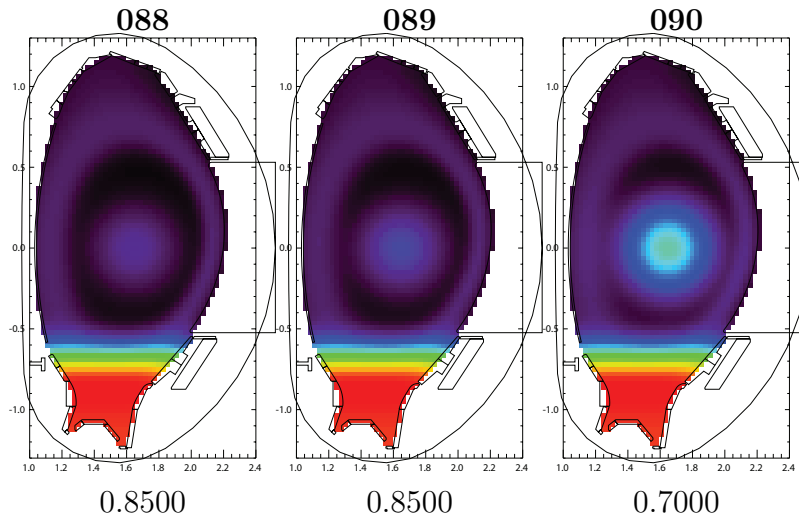
B Synthetic Emissivity Profiles





B Synthetic Emissivity Profiles





C Synthetic Bolometry Manual

This document is meant to give a short instruction for the usage of the Synthetic Bolometry program in order to create own emissivity profiles on ASDEX Upgrade and simulate the values measured by the foil bolometers that then can be used for the benchmarking of deconvolution algorithms. (Manual version from October 19, 2015; the latest version can be requested from stephan.gloeggler@ipp.mpg.de).

Requirements

The code requires IDL version 8.0 or higher (e.g. due to the use of null variables). Since it got written and tested under version 8.2, this version is highly recommended to ensure highest functionality.

The contour of the vessel is loaded automatically from a file which is stored in the same directory as the program. It has to have the form of the already existing file `30136.data.s` and its name has to have the form '`shotnumber.data.s`'. The program automatically detects new contour files and loads the correct file for each input `shot1`.

As this program was undergoing a lot of changes during its development it might happen that commands that are described in this manual do not work properly anymore or even throw errors. In this case don't hesitate to contact the author!

Description

The poloidal cross-section of the torus is covered by a grid, consisting of regular rectangles¹. Each area is assigned an emissivity value. The program will set all grid areas whose contour points are not within the vessel to zero. The emissivity profile can be created by using predefined tools for the most common radiation distributions, such as rings along the flux surfaces (also with asymmetries), point radiation etc. (see section C). The line-integrated brightness of the bolometer system's lines of sight is calculated by rastering them and applying a set of natural basis functions (distribution of the radiation over distance from origin, e.g. linear, exponentially or heaviside-like) on them. Also the total radiated power $P_{rad,tot}$ is calculated. The results can be output in a file as input for other programs.

Call

The program is called by

```
synthetic, infile = infile, nr, nz, shot1, style1, style2, outname = outname, $  
imgs = imgs, profile = profile, nostop = nostop, showme = showme
```

where

- n_r is the integer number of rectangles in r direction, n_z the integer number in z direction. The area covered by the rectangles is defined by the extremal positions of the initial and end points of the LOS.
- *shot1* is the shot that the LOS configuration is loaded from (this parameter is not to be confused with the later occurring one that is used in the commands of *style1!*).
- *style1* is an array of strings, defining the actual emissivity distribution (see sec. C).

¹Other grids may be defined by the user; to do this, substitute the procedure *create_rect_grid* (called only once in *synthetic.pro*) by another procedure whose output is an array of the grid areas contour lines.

- *style2* is a string which defines how the emissivity is seen by the LOS (see section C).
- the string parameter *outname* is optional and is the name of the *.synthetic* file in the sub-folder *data/out/* where the LOS' line-integrated brightness and $P_{rad,tot}$ are stored (see sec. C).
- the string parameter *imgs* is optional and indicates the names of the stored images. These are an image of the emissivity profile (in the folder *data/pictures/emprofiles*, ending *.emprofile.ps*) and an image of the LOS profile (in the folder *data/pictures/losprofiles*, ending *.LOS.ps*).
- the string parameter *profile* determines the name of the file that contains the numerical values of the emissivity profile (in the folder *data/emiss/*, ending *.emiss*).
- the boolean parameter *nostop* lets the program run without stop for any set value. If the parameter is not set, the program will stop and ask how to proceed before calculating the LOS measurement values. In this menu there is a possibility to save the call settings (n_r , n_z , *shot1*, *style1* and *style2*) for later reuse (in the folder *save/*, ending *.syntheticsave*).
- the boolean parameter *showme* determines if the emissivity distribution and the resulting LOS profile are shown for any set value. If the parameter is not set, the profiles will not be shown.
- the string parameter *infile* is the path of a *.syntheticsave* file and is set to call the *synthetic* program with the parameters stored in this file. In this case it is not necessary to set the parameters n_r , n_z , *shot1*, *style1* and *style2* as they will be ignored.

Reading Out the Files

To read out the files, two programs are provided:

read_synthetic.pro : Reads out a *.synthetic* file. Call:

read_synthetic, fname, shot, pradtot, cam_names, cam_channels, lines

Input	<i>fname</i>	File path
Output	<i>shot</i>	Shot from which LOS configuration was used
	<i>pradtot</i>	Total radiated power ($P_{rad,tot}$)
	<i>cam_names</i>	Names of the active cameras
	<i>cam_channels</i>	Number of channels per camera
	<i>lines</i>	Simulated measurement values, array filled up with -1

read_emiss_profile.pro : Reads out a *.emiss* file. Call:

read_emiss_profile, filename, emissivity, grid_ctl, shot1, showme = showme

Input	<i>filename</i>	File path
Output	<i>emissivity</i>	Emissivity of the single areas
	<i>grid_ctl</i>	Grid area contour points
	<i>shot1</i>	Shot from which LOS configuration was used
Optional	<i>showme</i>	Shows plot of the loaded emissivity profile

Emissivity profiles

The emissivity distribution in the vessel can be created by certain commands that are handed to the program as string elements of the array *style1*. Most of the commands are additive, i.e. can be used more than once and with different parameters. There is no maximum number of commands. Letter parameters are case insensitive.

An often recurring set of parameters is the one for the decay behavior with the distance d from the center of radiation. This behavior is characterized by a type of decay (see Table C.1), a parameter *par1* that indicates the emissivity value at the center of radiation (the *par1* of different commands are comparable to each other) and a parameter *par2* that has a different use for each type of decay (in general it can be seen as a kind of decay length for the emissivity).

Table C.1: Types of decay behavior

<i>type</i>	Name	Emissivity ϵ
<i>H</i>	Heaviside	$\epsilon = \begin{cases} par1 & (d \leq par2) \\ 0 & (d > par2) \end{cases}$
<i>R</i>	Exponential	$\epsilon = par1/d^{par2}$
<i>L</i>	Linear	$\epsilon = -d * par1/par2 + par1$
<i>G</i>	Gaussian	$\epsilon = \frac{1}{2\pi par2^2} e^{-\frac{d^2}{2par2^2}}$

For some commands magnetic field data are necessary. They can be taken from already existing shots. For this purpose those commands require the input of a shot number *shot* and a time *time* during this shot.

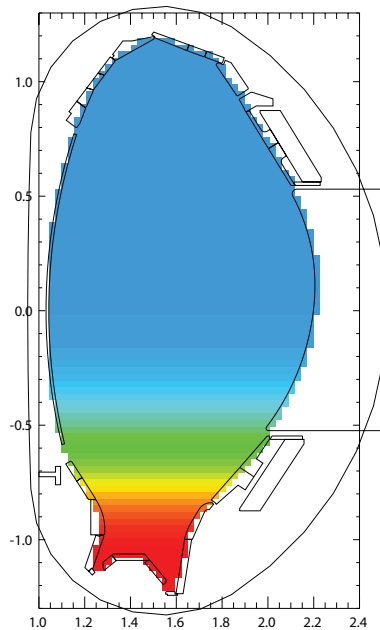
In the following subsections the commands, their parameters and properties are described. (Note: The colors of the emissivity and LOS profiles are always relative, i.e. two profiles are in general not comparable!)

Background radiation

The *b* command creates background radiation. The main chamber and the divertor can be assigned different values. The values are additive. To avoid the step between the two areas, smoothing can be performed at the end.

Call	<code>'b, (t, par_t), (m, par_m), (d, par_d), (s, par_s)'</code>
Parameters	Number: 1,3,5,7 or 9 Units: [m] b Create background radiation optional, order of the pairs does not matter: t Background radiation over all the tokamak par_t Value of t m Background radiation in the main chamber par_m Value of m d Background radiation in the divertor par_d Value of d s Smoothing of Divertor-Main chamber step par_s Value of s ($\in [0.01, 1]$; smoothing range)
Example call	<code>'b, d, 9, t, 5, s, 0.4'</code>

Example image



Point radiation

The p command creates a radiating point, decaying in a defining way.

Call	$'p, type, r0, z0, par1, par2'$
Parameters	Number: 6 Units: $[m]$ p Create point radiation type Type of decay: H, R, L, G (see Table C.1) r0 r coordinate of point location z0 z coordinate of point location par1 Emissivity value at $(r0/z0)$ par2 Length parameter for chosen decay
Example call	$'p, g, 1.5, 0, 1, 0.1'$
Example image	

X point radiation

The *x* command executes the *p* command at the location of the X point.

Call	<i>'x, shot, time, type, par1, par2'</i>
Parameters	Number: 6 Units: [m] x Create radiation around X point shot Shot to load X point coordinate from time Time to load X point coordinate from type Type of decay: <i>H,R,L,G</i> (see Table C.1) par1 Emissivity value at X point (center) par2 Length parameter for decay
Example call	<i>'x, 31648, 5.2, l, 10, 0.2'</i>
Example image	

Strike point radiation

The *s* command executes the *p* command at the location of the strike points. Inner and outer strike point can be switched on and off but the corresponding parameters always have to be defined.

Call	<i>'s, shot, time, in, type_i, par1_i, par2_i, out, type_o, par1_o, par2_o'</i>
Parameters	Number: 11 Units: [m] s Create radiation near strike points shot Shot to load magnetic flux data from time Time to load magnetic flux data from in Using inner strike point (isp)? (yes=1,no=0) type_i Type of decay, isp: <i>H,R,L,G</i> (see Table C.1) par1_i Emissivity value, isp (center) par2_i Length parameter for decay, isp out Using outer strike point (osp)? (yes=1,no=0) type_o Type of decay, osp: <i>H,R,L,G</i> (see Table C.1) par1_o Emissivity value, osp (center) par2_o Length parameter for decay, osp
Example call	<i>'s, 31113, 2, 1, h, 1, 0.05, 1, l, 2, 0.2'</i>
Example image	

Divertor leg radiation

The *l* command creates radiation that connects the strike points and the X point (not along the magnetic flux lines). Left and right divertor leg can be switched on and off. The one defined decay type is valid for both legs.

Call	<code>'l, shot, time, in, out, type, par1, par2'</code>
Parameters	Number: 8 Units: [m] l Create radiation along divertor legs shot Shot to load x point coordinate from time Time to load x point coordinate from in Taking inner divertor leg? (yes=1,no=0) out Taking outer divertor leg? (yes=1,no=0) type Type of decay: <i>H,R,L,G</i> (see Table C.1) par1 Emissivity value on the line par2 Length parameter for decay
Example call	<code>'l, 30789, 4.1, 1, 0, g, 1, 0.04'</code>
Example image	

Ring radiation

The *r* command creates radiation along a magnetic flux surface, i.e. will have the form of a ring. The distance over which the decay takes place is given in units of $[\rho_{pol}]$. A poloidal asymmetry can be introduced by defining two angles (in degrees) and the emissivity of this asymmetry *amp* (not necessary, only if the asymmetry is supposed to be additional). Radiation below the X point gets removed.

Call	<i>'r, shot, time, rho_pol, type, par1, par2(, deg1, deg2(, amp))'</i>
Parameters	Number: 7,9 or 10 Units: $[\rho_{pol}]$ (,Deg [°]) r Create radiation along magnetic flux surface shot Shot to load magnetic flux from time Time to load magnetic flux from rho_pol ρ_{pol} on which the ring is placed type Type of decay: <i>H,R,L,G</i> (see Table C.1) par1 Emissivity value at ρ_{pol} par2 Length parameter for decay optional, for partial ring: deg1 Start angle (0-360 degrees) deg2 End angle (0-360 degrees) amp (additional) emissivity of the asymmetry
Example call	<i>'r, 31648, 2.4, 0.9, g, 1, 0.15, 290, 130, 1'</i>
Example image	

Smoothing

The *smooth* command performs smoothing after the previous regular commands (*b,p,x,s,l,r*) have been executed. It substitutes every grid points emissivity by the mean value of all its neighbors in distance *par_s*.

Call	<i>'smooth, par_s'</i>
Parameters	Number: 2 Units: [m] smooth Create radiation around x point par_s Smooth parameter
Example call	<i>'smooth, 0.1'</i>

Randomizing

The *random* command varies the emissivity randomly around the maximum percentage \pm *par_rand*. The *random* command is executed after the regular commands (*b,p,x,s,l,r*) and the *smooth* command.

Call	<i>'random, par_rand'</i>
Parameters	Number: 2 Units: [%] random Randomize the emissivity profile par_rand Percentage of randomness
Example call	<i>'random, 0.2'</i>

Maximum emissivity

The *max* command scales the emissivity profile so that its maximum value will be *par_max*. The *max* command is executed after the regular commands (*b,p,x,s,l,r*), the *smooth* command and the *random* command. It can not be executed together with the *prad* command!

Call	<i>'max, par_max'</i>
Parameters	Number: 2 Units: [W/m ³] max Define maximum emissivity par_max New maximum emissivity
Example call	<i>'max, 4900000'</i>

Set P_(rad,tot)

The *prad* command scales the emissivity profile so that $P_{rad,tot}$ will be *par_tot*. The *prad* command is executed after the regular commands (*b,p,x,s,l,r*), the *smooth* command and the *random* command. It can not be executed together with the *max* command!

Call	<i>'prad, par_tot'</i>
Parameters	Number: 2 Units: [W] prad Define $P_{rad,tot}$ par_tot New $P_{rad,tot}$
Example call	<i>'prad, 10000000'</i>

C Synthetic Bolometry Manual

The emissivity values will always be scaled in a way that the maximum value is the one given in *par1*. Negative values for *par1* are possible. Only after having executed all the commands, negative emissivity values will be set to zero.

If the number of input parameters for a command is wrong, the program will stop and show the commands manual (which contains the commands parameters and their meaning). This means that for seeing the manual of a command it is only necessary to input a string with the correspondent letter, e.g. '*r*' for the manual of the ring command.

Before the line-integrated brightness of the LOS is calculated, the user has the opportunity to see the emissivity distribution. To abort and correct the input, type "retall". To proceed, type ".c".

Calculation of the lines of sight

Weighted calculation

The line-integrated brightness is calculated by subdividing each LOS into 1000 sections with length $l_i/1000$. For the center of each subsection the neighboring 4 grid center points and their distance d_j to the LOS subsections center are calculated. The brightness B_i of the i -th LOS is then given by

$$B_i = \sum_{j=1}^N \mathbf{G}_{i,j} \cdot \epsilon_j = \sum_{j=1}^N \left(\sum_{m=1}^{1000} \frac{l_i}{1000} \cdot \frac{f(d_m)}{\sum_{k=1}^N f(d_k)} \right) \cdot \epsilon_j$$

The model function $f(d)$ can be chosen over the input parameter *style2* as follows: *style2* is a string, consisting of a letter S which describes the type of model function (case insensitive) and a number p which is a parameter for the model function. They are separated by a comma. See Table C.2 for more details, parameter values (tested with a 46x84 rectangular grid) and examples.

Table C.2: Usage and examples of the model functions.

Model	S	Function $f(d)$	Parameter p	Example call
Constant	C	$f(d) = p$	$p \in [0, \infty]$	'c,2'
Hyperbolic	R	$f(d) = 1/d^p$	$p \in [0.01, 2]$	'r,0.1'
Linear	L	$f(d) = -d/p + 1$	$p \in [0.01, 5]$	'l,0.2'
Gaussian	G	$f(d) = \frac{1}{2\pi p^2} e^{-\frac{d^2}{2p^2}}$	$p \in [0.01, 2]$	'g,0.2'
Heaviside	H	$f(d) = \begin{cases} 1 & (d \leq p) \\ 0 & (d > p) \end{cases}$	$p \in [0, 1]$	'h,0.2'

Annotations to Table C.2:

Constant: Equal weight for every grid point (independent of the distance)

Linear: Negative values of $f(d)$ are set to zero

Heaviside: Equal weight for every grid point inside circle of radius p

For certain parameter values IDL will throw the warning "Program caused arithmetic error: Floating underflow", which can be neglected if the parameters are chosen as described above. Other formats than described in Table C.2 (e.g. defining more than one model function) will cause errors or wrong results of the program.

Heaviside-like calculation

It is also possible to assume equally distributed radiation within the grid areas. The style to chose is called (without additional parameters) '*H2D*'. The program then checks for every subsection of the LOS in which grid area the subsections center is located and only accounts this area to the total brightness of the line. This model can require more calculation time than those mentioned above (giving similar results).

Randomize values

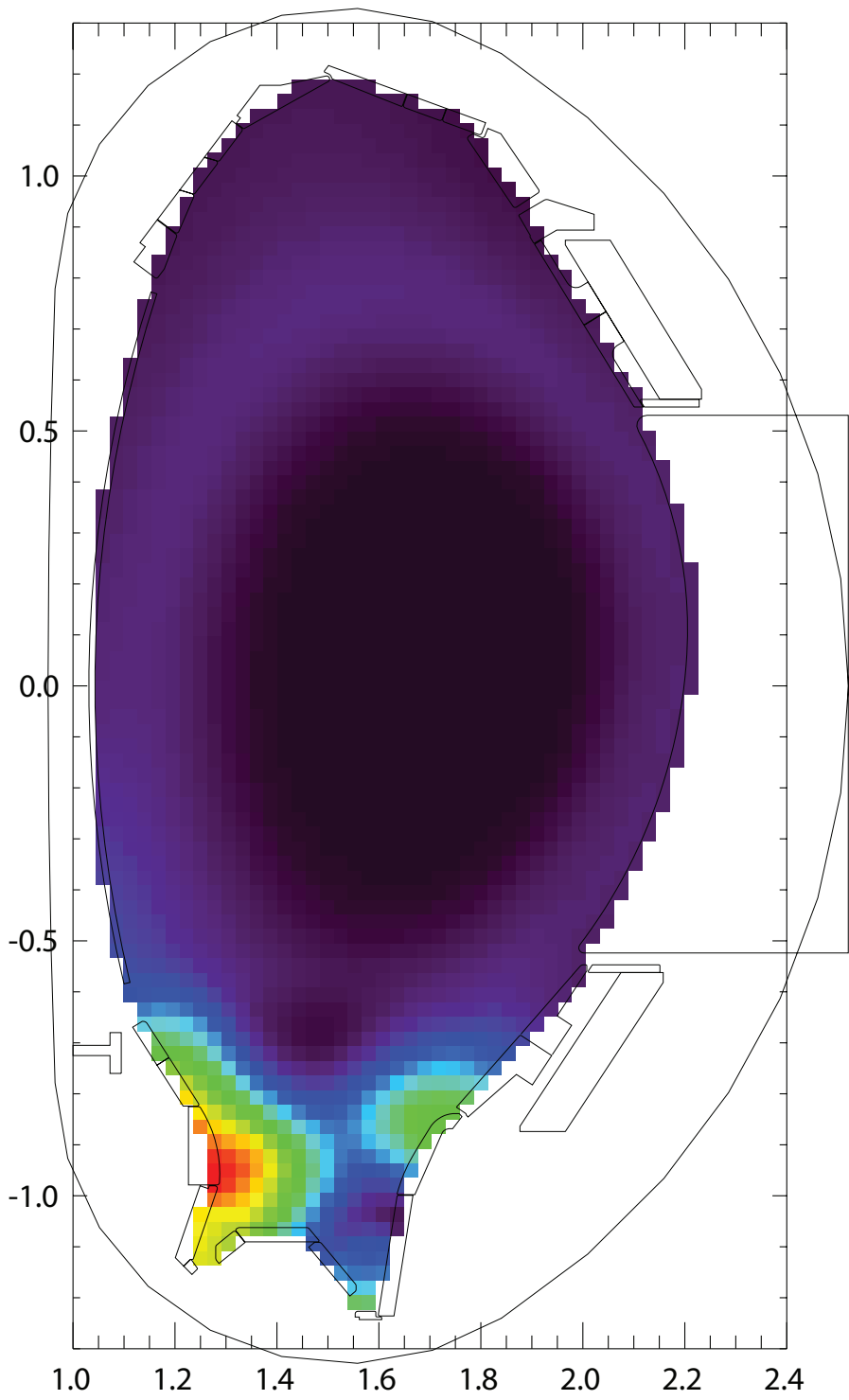
The command for a later randomizing of the calculated LOS values is handed over in *style2* as well. To do so, it is only necessary to add a semicolon ; and a parameter to *style2*. The parameter indicates the maximum percentage that the values of the LOS can be varied. For example, $r, 0.3; 0.1$ indicates that the emissivity value of each grid area will be between 90 and 110 % of its original value.

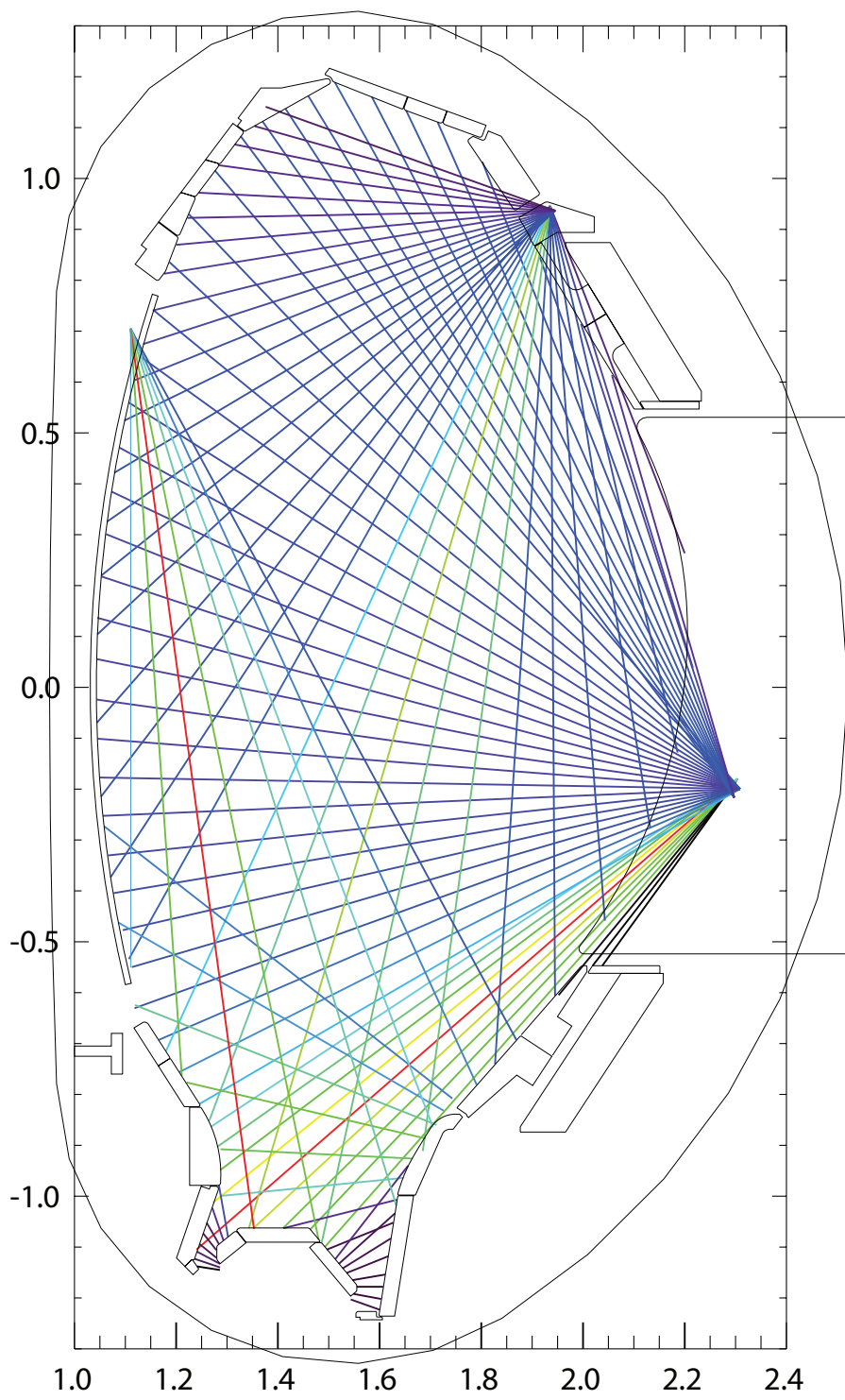
Example

An example with as much commands as possible shall be used here to create a realistic emissivity profile. The input command is as follows (using the IDL convention to break lines with the Dollar symbol \$ to make it more illustrative):

```
synthetic, 46, 84, 31648, $  
['max, 6390000', $  
's, 30732, 7, 1, g, 0.9, 0.04, 1, g, 2, 0.02', $  
'p, g, 1.3, -0.92, 1.1, 0.1', $  
'x, 30732, 7, g, 0.5, 0.05', $  
'r, 30732, 7, 1.12, g, 0.4, 0.05, 180, 300', $  
'p, g, 1.20, -0.72, 1, 0.05', $  
'p, g, 1.7, -0.85, 0.9, 0.09', $  
'b, t, -0.1, m, 0.15', $  
'p, g, 1.55, -0.87, 0.3, 0.05', $  
'p, g, 1.22, -0.85, 0.7, 0.05', $  
'smooth, 0.1', $  
'p, g, 1.85, -0.75, 0.4, 0.05', $  
'l, 30732, 7, 1, 1, g, 0.4, 0.03', $  
'r, 30732, 7, 0.98, g, 0.1, 0.1'], $  
'h2d', img = 'docu_example', file = 'docu_example'
```

On the following pages the reader can find the emissivity profile, the LOS profile and the measurement values of the LOS (CH = Channel, LIB = Line-integrated brightness (kW/m²)) and of $P_{rad,tot}$.





C Synthetic Bolometry Manual

Camera	CH	LIB	CH	LIB	CH	LIB
FHC	1	0	17	573	33	560
	2	0	18	538	34	587
	3	57	19	518	35	620
	4	1427	20	496	36	656
	5	1512	21	477	37	693
	6	1711	22	466	38	711
	7	1959	23	455	39	729
	8	2516	24	450	40	749
	9	2046	25	449	41	770
	10	1609	26	453	42	753
	11	1311	27	469	43	733
	12	1118	28	481	44	715
	13	980	29	491	45	664
	14	904	30	503	46	563
	15	821	31	518	47	470
	16	685	32	537	48	386
Camera	CH	LIB	CH	LIB	CH	LIB
FVC	1	285	17	666		
	2	472	18	662		
	3	585	19	649		
	4	616	20	626		
	5	624	21	586		
	6	636	22	546		
	7	761	23	505		
	8	1293	24	467		
	9	1296	25	428		
	10	1869	26	396		
	11	1247	27	370		
	12	1017	28	348		
	13	776	29	319		
	14	726	30	300		
	15	684	31	300		
	16	668	32	247		

Camera	CH	LIB	Camera	CH	LIB
FLX	1	166	FDO	1	178
	2	351		2	143
	3	1163		3	101
	4	1364		4	137
	5	1410		5	168
	6	1263		6	188
	7	910		7	191
	8	870		8	293
Camera	CH	LIB	Camera	CH	LIB
FDI	1	555	FHS	1	703
	2	338		2	886
	3	240		3	1141
	4	209		4	1229
	5	212		5	1695
	6	253		6	2585
	7	212		7	1421
	8	0		8	917

$$P_{rad,tot} = 14.4430 \text{ MW}$$

Necessary files

- check_val_grid.pro
- create_emiss.pro
- create_rect_grid.pro
- distro_func.pro
- find_bol_config.pro
- get_bfield.pro
- heaviside.pro
- intersection.pro
- output.pro
- poly_func.pro
- rad_szen_b.pro
- rad_szen_g.pro
- rad_szen_l.pro
- rad_szen_p.pro
- rad_szen_r.pro
- rad_szen_s.pro
- rad_szen_x.pro
- read_bol_config.pro
- read_signal.pro

- schnittpunkt.pro
- synthetic.pro
- vessel.pro
- 30136.data.s or other file(s) with the vessel contour data

To read out the output files, the following programs are provided:

- read_synthetic.pro
- read_emiss_profile.pro

Acknowledgements

This work would not have been possible without the support of many people:

First of all, I would like to thank Matthias Bernert for his supervision over my work, his many helpful pieces of advice and competent answers on putative short questions. I would like to thank Thomas Eich for motivating me to go into plasma physics and for assessing my work. I'm very grateful to Frank Jenko for giving me the opportunity to do my master thesis at the IPP.

I would like to express my deep appreciation to Christoph Fuchs, Tomáš Odstrčil, Ralph Dux, Felix Reimold, Arne Kallenbach, Till Sehmer, Athina Kappatou and Thomas Pütterich for helping me with their wide expertise.

I thank my office mates Patrick Astfalk, Alexander Lessig, Nils Leuthold, Thomas Hayward and Branka Vanovac for the friendly and inspirational working atmosphere.

I would like to thank Michael Faitsch, Michael Griener, Felician Mink and Golo Fuchert for their companionship during my study in Ulm and at the IPP, for their help and advice and the diverting board game evenings.

Special greetings go to the students from all over the world that I was fortunate to get to know at Siena and Pisa. You all made my year in Italy unforgettable and showed me my way in life.

Studying can be hard sometimes, but thanks to my fellow students from the University of Ulm it was always a joy. Thank you for all your support and friendship! Particular thanks to Thomas Brenner for many deep conversations about everything under the sun.

I'm deeply grateful to my friends from Ulm and Oberkirchberg which supported me in all this time, some already since we were still children.

Acknowledgements

Eine ständige Inspiration für meine Begeisterung für Wissenschaft und Technik war zweifelsohne die Werkstatt meines Opa Josef. Ganz besonders danken möchte ich meinen Eltern und meiner Schwester Verena dafür, dass sie mich so gut aufs Leben vorbereitet und mich immer unterstützt haben. Ein besonderer Dank geht an meine Freundin Monica, die auch in schwierigen Momenten für mich da war.